

resonant interface or quantum well resonant states can be put forward (it can be analogous to that of virtual bound states in bulk materials). Numerical calculations of the electronic structure and electron scattering at rough interfaces would be of great interest. Finally, although most present models take into consideration only a periodic distribution of *scattering potentials*, some attempts have recently been made to consider also the influence of the *periodic interface potential of the superlattice* (Sects. 2.2.4a, b). The interplay between scattering and periodic potentials could be an important point leading to a better understanding of the effectiveness of certain interfaces.

Acknowledgements. One of us (A.F.) acknowledges support from the European Economic Community (Esprit project BRA 6146) and the NATO (grant number 5-2-05/RE 890599).

2.3 Investigation of Exchange Coupled Magnetic Layers by Scanning Electron Microscopy with Polarization Analysis (SEMPA)

D.T. PIERCE, J. UNGURIS, and R.J. CELOTTA

Artificially layered magnetic structures offer the promise of being able to tailor transport and magnetic properties to fit specific needs. For example, two ferromagnetic layers separated by a nonferromagnetic interlayer can be exchange coupled such that the magnetic moments in the two ferromagnetic layers are parallel (ferromagnetic exchange coupling) or antiparallel (antiferromagnetic exchange coupling) depending on the interlayer material and its thickness [2.149, 150]. Two magnetic layers that are antiferromagnetically coupled in the absence of an applied magnetic field can be forced into ferromagnetic alignment by the application of a sufficiently strong magnetic field. Accompanying the change from antiferromagnetic to ferromagnetic alignment is a large reduction in the electrical resistance of the multilayer structure [2.151, 152]. This "giant" magnetoresistance (discussed by *Fert* and *Bruno* in Sect 2.2 and *Parkin* in Sect. 2.4) is of interest for applications to magnetoresistive recording heads and sensors and has stimulated much of the activity in this field. The magnetoresistance and the applied field required to obtain ferromagnetic alignment of the magnetic layers can be varied widely by varying the material of the ferromagnetic layers, the interlayer material, and the interlayer thickness.

For many combinations of magnetic layer materials and nonmagnetic interlayer materials, the exchange coupling has been found to oscillate from ferromagnetic to antiferromagnetic with changing nonmagnetic layer thickness [2.149, 153]. In the case of Gd/Y multilayers [2.149], the localized rare earth magnetic moments allow the long range oscillatory exchange coupling to be adequately explained [2.154] by the Ruderman-Kittel-Kasuya-Yosida (RKKY) [2.155] interaction. When the magnetic layer is a transition metal, the less localized nature of the magnetic moments complicates the theory (Sect. 2.1).

There are many different theoretical approaches including RKKY-like models between planes of local moments [2.156–160], free electron-like particle-in-box models [2.161, 162], tight-binding models with magnetic interaction [2.163–165], and self-consistent electronic structure calculations [2.166]. There is considerable ongoing experimental effort to elucidate the nature of the magnetic coupling. The strength of the coupling can be measured by ferromagnetic resonance (FMR), Brillouin light scattering (BLS), and, in the antiferromagnetic coupling region, by the surface magneto-optic Kerr effect (SMOKE) (Sects. 3.1, 3.2, and 4.1 respectively). In favorable circumstances, oscillations in the exchange coupling over a limited range have been observed with these techniques.

Scanning Electron Microscopy with Polarization Analysis (SEMPA) has proved particularly well-suited to determining the period (or periods) of oscillation of the exchange coupling between magnetic layers. SEMPA images the magnetization of the top few layers of a magnetic material by measuring the spin polarization of secondary electrons excited from the material by the electron beam in a scanning electron microscope (SEM) as described in Sect. 2.3.1. For comparison to theory, measurements should be made of materials which are perfect crystals with sharp interfaces between the layers. This challenge to achieve perfection is very nearly met by growing epitaxial Cr films on Fe(100) single crystal whiskers, as described in Sect. 2.3.2a. The period of the oscillation in exchange coupling as a function of interlayer thickness can be determined accurately only if the interlayer film thickness can be varied nearly continuously in a reproducible manner and accurately measured. This is achieved by using spatially resolved reflection high energy electron diffraction (RHEED) to measure each atomic layer increment in the thickness of the interlayer material which is grown so the thickness varies linearly with distance along the substrate like a wedge. The observation of two different oscillation periods in the exchange coupling of Fe/Cr/Fe(100), their sensitivity to interlayer growth conditions, and the connection of the periods to Fermi surface nesting vectors are discussed in Sect. 2.3.2b. Additionally, the agreement between the two oscillation periods measured for a Ag spacer layer and the predictions based on the Ag Fermi surface are briefly discussed. Another coupling, biquadratic exchange coupling, is discussed in Sect. 2.3.2c and a brief summary is given in Sect. 2.3.2d.

2.3.1. The SEMPA Technique

2.3.1.1 Principle

The SEMPA technique (Scanning Electron Microscopy with Polarization Analysis) relies on the fact that the secondary electrons emitted from a ferromagnet have a spin polarization which reflects the net spin density in the material which in turn is related to the magnetization. The spin part of the magnetization

is

$$M = -\mu_B(n_{\uparrow} - n_{\downarrow}), \quad (2.76)$$

where $n_{\uparrow}(n_{\downarrow})$ are the number of spins per unit volume parallel (antiparallel) to the particular direction. Recall that the electron spin magnetic moment μ (units of Bohr magneton, μ_B) and the electron spin s (units of $\hbar/2$) point in opposite directions $\mu = -\mu_B s$. The spin part of the magnetization is a close approximation to the total magnetization in a transition metal ferromagnet in which the orbital moment is quenched by the cubic crystal field.

The spin polarization of the secondary electrons emitted from a ferromagnetic sample is a vector quantity. For the purposes of SEMPA it is adequate to consider each component of the polarization separately. The polarization along, for example, the z direction is

$$P_z = (N_{\uparrow} - N_{\downarrow}) / (N_{\uparrow} + N_{\downarrow}), \quad (2.77)$$

where $N_{\uparrow}(N_{\downarrow})$ are the number of electrons with spins parallel (antiparallel) to the z direction. The polarization may have values $-1 \leq P \leq 1$.

The first measurements [2.167] of the energy distribution of the spin polarization of secondary electrons emitted from a ferromagnet were made on the ferromagnetic glass $\text{Fe}_{81.5}\text{B}_{14.5}\text{Si}_4$ and are shown in Fig. 2.35. The lower part of the figure shows the number $N(E)$ of secondary electrons as a function of kinetic energy. The familiar low energy peak in the secondary electron intensity distribution is due to the secondary electron cascade process which excites many electron-hole pairs in the valence band. To the extent that the cascade electrons represent a uniform excitation of electrons from the valence band, the expected polarization is

$$P = n_B / n_v, \quad (2.78)$$

where n_v is the total number of valence electrons per atom. The number of Bohr magnetons per atom, n_B , is the difference in the number of majority (spin antiparallel to the magnetization) and minority spins per atom. This simple model predicts polarizations of 28%, 19%, and 5% for Fe, Co, and Ni, respectively. These values agree reasonably well with polarizations measured for kinetic energies between 10 and 20 eV for Fe [2.168], Co [2.168], and Ni [2.169].

The measured secondary electron polarization is not constant as a function of kinetic energy and increases below about 10 eV as seen in the top part of Fig. 2.35. From the measurements [2.168, 169] of Fe, Co, and Ni it is known that the increase at low energy is an enhancement over the predicted values, n_B / n_v . The enhancement is due to the spin dependent filtering of the low energy electrons [2.170, 171]. As the kinetic energy becomes smaller, the probability that the electron will lose energy and drop down into an unoccupied state below the vacuum level increases. In a ferromagnet, there are more minority spin unoccupied states so minority spin electrons are preferentially removed from the secondary electron distribution thereby making the polarization more positive.

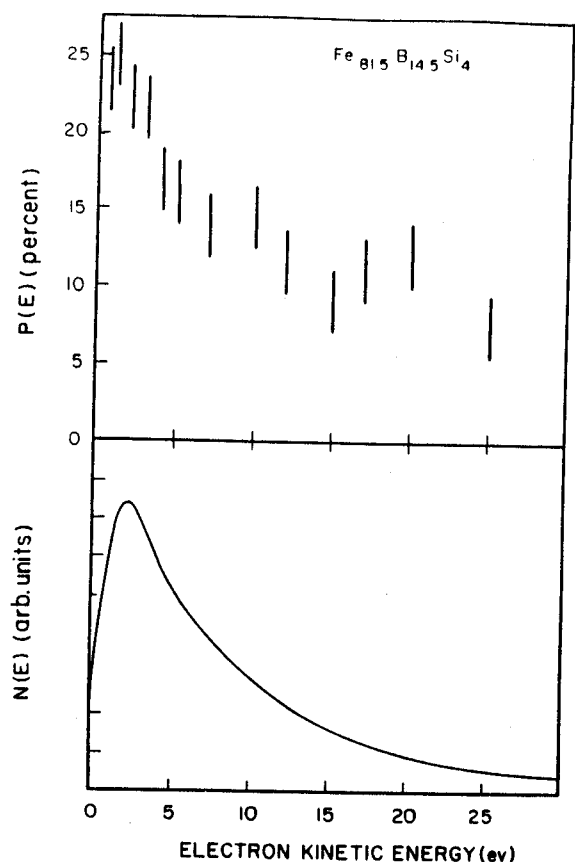


Fig. 2.35. Bottom: The energy distribution of secondary electrons emitted from the amorphous ferromagnetic $\text{Fe}_{81.5}\text{B}_{14.5}\text{Si}_4$. Top: The spin polarization of the secondary electrons as a function of kinetic energy. (From [2.167])

If the spin density which gives rise to M in (2.76) is uniformly sampled in the secondary electron distribution and the electrons are emitted without changing their polarization, then P is related to M as in (2.78). In practice, the constant of proportionality is not known precisely and will depend on the electron states sampled and on the range of kinetic energies measured, as indicated by Fig. 2.35. It may thus be different for two materials that have spin densities distributed differently in energy that therefore contribute differently to the polarization of the secondary electron distribution. Thus, the polarization of secondary electrons can be taken to be proportional to the magnetization, but it is in general not possible to deduce quantitative values for the surface magnetization or the corresponding surface magnetic moments. In other polarized electron spectroscopies, when the electrons excited to specific states are selected in an energy and angle-resolved measurement the proportionality of P and M may be even more complex (Volume I, Sects. 2.1 and 2.2).

Another important feature of the secondary electrons is that they are emitted from a region near the surface of the material. The energy of the incident electron beam is deposited in the sample to a significant depth, of the order of hundreds of nanometers for incident energies of a few keV [2.172]. However,

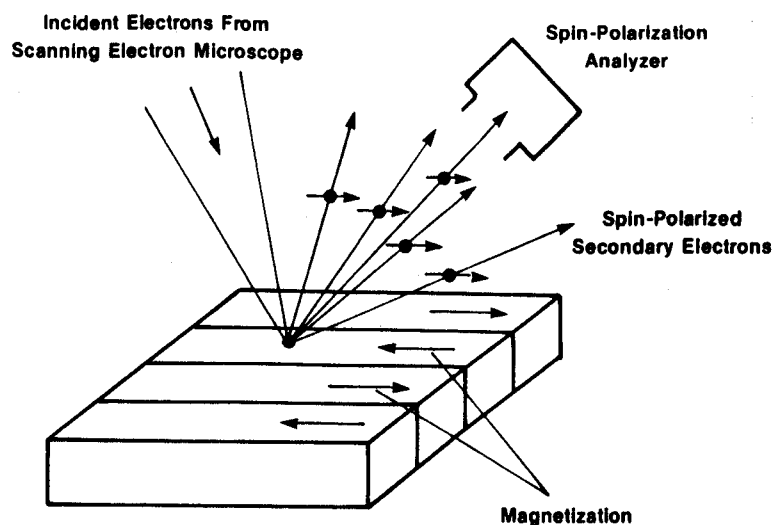


Fig. 2.36. The principle of Scanning Electron Microscopy with Polarization Analysis (SEMPA): The spin polarization of the secondary electrons generated by the scanned electron beam is measured to give an image of the specimen magnetization

only those electrons that are close enough to the surface can escape before losing sufficient energy that they fall below the vacuum level. For spin polarized secondary electrons, the $1/e$ sampling depth, or average attenuation length, is of order 1 nm, ranging from about 0.5 nm for a transition metal like Cr [2.173] to about 1.5 nm for a noble metal like Ag [2.174].

The measurements [2.167] of the secondary electron spin polarization shown in Fig. 2.35 provided a significant stimulus to the development of SEMPA. The results showed that there were many low energy electrons and that they have a sizeable polarization. Furthermore, it was clear that the spin polarization of the secondary electrons was closely related to the net spin density, and hence the magnetization, near the surface of the material. Therefore, it was suggested [2.167, 175] that by exciting the electrons with a well focused beam in a scanning electron microscope (SEM) one could obtain a spatially resolved magnetization measurement at the sample. This technique [2.176, 177], now called SEMPA, is illustrated schematically in Fig. 2.36. In the SEM, the incident beam is rastered across the sample. The spin polarization analyzer measures the polarization of the secondary electrons and the number of secondary electrons simultaneously to give a magnetization image and a topographic image of the sample.

2.3.1.2 Apparatus

The essential elements of a SEMPA apparatus are 1) a SEM column to form the focused incident electron beam, 2) an ultrahigh vacuum chamber with instru-

mentation for surface preparation and analysis, 3) electron spin polarization analyzers, 4) transport electron optics to collect and transport the emitted secondary electrons from the sample to the spin analyzer, and 5) a data storage and image processing system to transform raw data to magnetization images. The SEMPA apparatus [2.178, 179] used in obtaining the results described here is shown schematically in Fig. 2.37.

The choice of electron microscope and specimen chamber are constrained by the surface sensitivity of SEMPA which requires an ultrahigh vacuum surface analysis environment. The vacuum must be good enough so that background gases do not adsorb significantly on the sample surface and diminish the magnetic contrast. Conventional surface science preparation techniques like ion

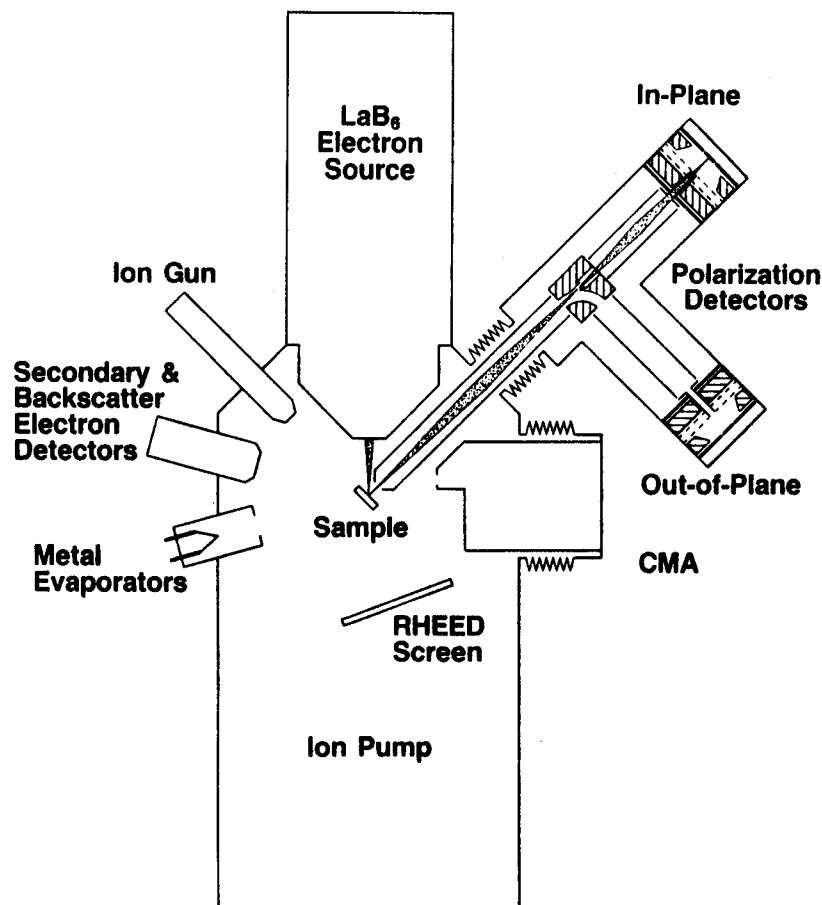


Fig. 2.37. Schematic drawing of the NIST SEMPA apparatus. The cylindrical mirror analyzer (CMA) and spin polarization analyzers are mounted on bellows. The ion gun, secondary and backscatter electron detectors, and metal evaporators are not shown in their true position

bombardment and annealing, and analysis techniques like Auger spectroscopy, to measure sample surface chemical composition, are desirable. Such requirements are met most conveniently by commercial scanning Auger microprobes to which SEMPA can be added. In our apparatus, shown in Fig. 2.37, the cylindrical mirror analyzer (CMA) used for Auger spectroscopy can be retracted to allow insertion of the SEMPA electron collection and transport optics close to the sample. The evaporation sources, which have been added, are shown schematically in Fig. 2.37 but actually are positioned near the Auger analyzer so that either SEMPA or Auger spectroscopy can be carried out during evaporation. A phosphor screen below the sample stage allows reflection high energy electron diffraction (RHEED) measurements to be carried out when the sample is tilted so the SEM beam is at grazing incidence.

Owing to the inefficiency of existing spin polarization analyzers, it is important to have a high brightness cathode in the SEM electron gun. In our apparatus, SEMPA images can be obtained in a reasonable time with a minimum beam current of 1 nA. Our apparatus has a LaB_6 thermionic emission cathode which produces the required current in a beam diameter of 50 nm. For future higher resolution measurements, an apparatus with a thermally assisted field emitter that produces 1 nA in a beam of 10 nm diameter will be used. The choice of incident electron beam energy is a tradeoff between resolution and signal intensity. With increasing beam energy, a smaller beam diameter is possible but the secondary yield decreases. Under our typical operating conditions, a 10 keV incident electron beam is used which produces a secondary yield that is approximately 20% of the incident beam current. Another tradeoff is between a shorter working distance (between the sample and the SEM objective lens) which leads to a smaller beam diameter and a longer distance which leads to a smaller magnetic field (from the objective lens) at the sample. Some minimum working distance is also necessary to extract the polarized secondary electrons. A reasonable compromise is a working distance of 10 mm and a stray field at the sample of 1 Oe (80 A m^{-1}) or less.

Transport optics must efficiently collect the spin polarized secondary electrons emitted from the sample surface and deliver them at the correct energy to the spin polarization analyzer. Additionally, the transport optics should map the spot under the scanned electron beam on the sample surface, which determines the source of polarized electrons, onto the scattering target of the spin analyzer in such a way as to minimize spurious instrumental asymmetries in the analyzer. In our apparatus, the front end of the transport optics is biased at $\pm 1500 \text{ V}$ relative to the sample to collect the low energy secondary electrons. The transport optics are designed to transmit the secondary electrons with initial kinetic energies between 0 and 8 eV to the spin analyzer. The transport optics also contain descanned deflectors which prevent the motion of the SEM beam on the sample, i.e. the moving secondary electron source, from being transmitted to the spin analyzer which could introduce instrumental asymmetries for large area scans. As seen in Fig. 2.37, the transport optics also contain a 90° spherical deflector to shift the beam to an orthogonal spin analyzer. Each spin analyzer

can measure the two components of polarization transverse to the electron beam. Out-of-plane magnetization at the sample leads to a component of polarization along the electron beam. The spherical deflector changes the electron momentum without (at these energies) changing the electron spin direction so the orthogonal analyzer measures the component of polarization out-of-plane as well as one in-plane component. The redundant measurement of the in-plane component by both spin analyzers provides a monitor of the stability of the polarization sensitivity of each.

The spin analyzer is a key element of the SEMPA apparatus. The characteristics of the wide range of available spin analyzers have been compared [2.180, 181] and the application of several of them to SEMPA has been discussed [2.178]. A number of features are desirable in a spin analyzer for a SEMPA measurement: 1) The highest possible efficiency is required. 2) The electron optical phase space of the spin analyzer must be appropriately matched to the phase space of the secondary electrons to be analyzed. 3) The spin analyzer should accept a range of secondary electron energies to take advantage of the high polarization, high intensity peak in the secondary electron distribution (Fig. 2.35). 4) The spin analyzer should have maximum immunity to false apparatus asymmetries resulting from changes in position and angle of the electron beam entering the analyzer. 5) The spin analyzer should minimally perturb the operation of the SEM. 6) The SEMPA measurement is sufficiently demanding that the spin analyzer must be reliable and easy to use.

The spin-orbit interaction is the spin dependent interaction which is the basis of the spin sensitivity in the most commonly used spin analyzers [2.182]. When an electron scatters from the central potential of a high atomic number atom, there is an interaction between the electron's spin and its orbital angular momentum about the scattering center. This spin-orbit interaction introduces a difference in the scattering cross sections depending on whether the spin of the electron is parallel or antiparallel to the scattering plane normal. The normal to the scattering plane, \mathbf{n} , is defined in terms of the incident and final electron wavevectors, \mathbf{k}_i and \mathbf{k}_f , which lie in the scattering plane as, $\mathbf{n} = (\mathbf{k}_i \times \mathbf{k}_f) / |\mathbf{k}_i \times \mathbf{k}_f|$. The scattering cross section can be written

$$\sigma(\theta) = I(\theta)[1 + S(\theta)\mathbf{P} \cdot \mathbf{n}], \quad (2.79)$$

where \mathbf{P} is the beam polarization, $I(\theta)$ is the angular distribution of back-scattered electrons, and $S(\theta)$ is the Sherman function for the spin analyzer scattering target [2.182]. The Sherman function is a measure of the strength of the spin-dependent scattering which depends on the target material and the beam energy and angle. To measure the polarization of the beam, one measures the asymmetry A_s in the number of electrons scattered to the left, N_L , and to the right, N_R , relative to the incident beam direction:

$$A_s = (N_L - N_R) / (N_L + N_R) = PS. \quad (2.80)$$

Here S is the integrated Sherman function for the range of angles collected.

For a measurement limited by counting statistics, the efficiency of a spin analyzer is described by the figure of merit

$$F_s = S^2 I / I_0, \quad (2.81)$$

where I_0 is the beam intensity incident on the spin analyzer scattering target. For typical analyzers [2.180, 181], S lies between 0.1 and 0.3, and I/I_0 is in the range 10^{-2} – 10^{-4} . The figure of merit is of the order of 10^{-4} for the most efficient spin analyzers. The uncertainty δP in the polarization measurement [2.182] of a beam of N electrons is $\delta P = (NF_s)^{-1/2}$. Compared to an intensity measurement, where the relative uncertainty is $\delta N/N = N^{-1/2}$, the relative uncertainty in the polarization measurement is $\delta P/P = (P^2 NF_s)^{-1/2}$. Thus, compared to an intensity measurement, a polarization measurement with the same statistical precision will take $P^{-2} F_s^{-1}$, or at least 10^4 times, as long to make. Hence there is considerable emphasis on the efficiency of the spin analyzers in a SEMPA measurement.

No single analyzer fully meets all of the other requirements on spin analyzers in addition to efficiency. For example, the high energy (100 keV) Mott analyzer [2.182] has the highest electron optical acceptance, but because of the high voltage requirement, it is much larger and more cumbersome than low energy spin analyzers. Nevertheless, the first SEMPA measurements [2.176, 183] were made by attaching a high quality scanning electron gun to a 100 keV Mott

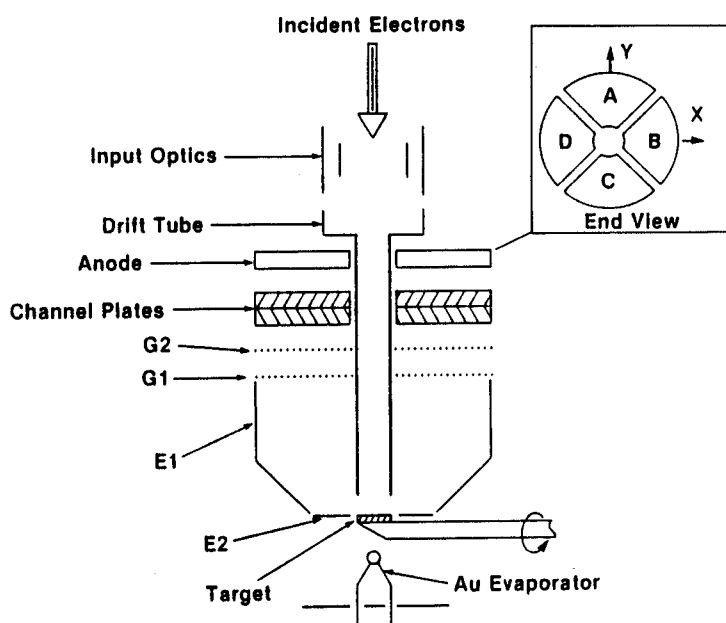


Fig. 2.38. A cross section of the low energy diffuse scattering spin analyzer used for SEMPA. The divided anode assembly is shown in the inset as viewed from the Au target

analyzer. Our approach was to develop a high efficiency, compact low energy spin analyzer which could be attached directly to an existing SEM [2.177, 180, 184]. In addition to the apparatus described here, SEMPA apparatuses currently in operation include those using [2.176, 185] high energy Mott analyzers and one using [2.186] a low energy electron diffraction (LEED) analyzer. The specifications and relative merits of the various analyzers for SEMPA have been previously discussed [2.178, 180]. Recently a high figure of merit spin analyzer based on exchange scattering has been introduced [2.187]; however, when account is taken of its acceptance phase space and limitations on the range of energies accepted by it, the overall efficiency for SEMPA is only marginally higher than the best of the other analyzers discussed. Moreover, at this stage of its development it requires a significantly greater effort to use. Here we will focus our further discussion on the low energy diffuse scattering analyzers shown in Fig. 2.37.

A schematic of the low energy diffuse scattering analyzer [2.180, 188] is shown in Fig. 2.38. In this detector a 150 eV beam is incident on an evaporated polycrystalline Au target. The electrons, which are diffusely scattered by the Au target, are deflected by the electrode E1 such that their trajectories are approximately normal to grids G1 and G2, which filter out the low energy secondaries generated at the Au target. The electrons passing the grids are multiplied by the channel plates and are detected by the anode which is divided into four equal quadrants as shown in the inset of Fig. 2.38. Two orthogonal components of the transverse polarization are measured simultaneously:

$$P_x = (1/S)(N_C - N_A)/(N_C + N_A), \quad (2.82a)$$

$$P_y = (1/S)(N_B - N_D)/(N_B + N_D), \quad (2.82b)$$

where N_i is the number of electrons counted by quadrant i . The spin analyzer is very efficient having a figure of merit of 2×10^{-4} which does not change over the 8 eV energy width of the electron beam [2.180, 188]. The electron optical acceptance is well-matched to the phase space of the electrons to be measured. The spin analyzer is reliable, compact and readily interfaced to the SEM electron optical column without destabilizing the column itself.

A common problem with any spin analyzer is the elimination of any false polarization signals due to instrumental asymmetries. Instrumental asymmetries that remain constant, such as due to a mechanical misalignment or due to a difference in electronic gain in a signal channel, can be measured and accounted for. More troubling are asymmetries resulting from actual movement of the incident beam in position or angle at the spin analyzer target. The electron trajectories at the spin analyzer can vary because of the scanning of the SEM beam on the sample, because of variations in the extraction electric field at the sample owing to the sample geometry, and because of variation in topography, work function, or stray magnetic field in the extraction region. Asymmetries due to the SEM beam scanning on the sample are minimized by the descans in the transport optics. Also, it is possible to compensate the asymmetry caused by a

displacement of the electron beam at the Au target by causing that beam displacement to be accompanied by a change in angle that causes an equal and opposite asymmetry [2.188]. The input optics are designed to do just this. By these means, instrumental asymmetries are reduced to a negligible level for most SEMPA measurements. The beam polarization as defined in (2.77) contains the simultaneously measured beam intensity and thus should be insensitive to variations in intensity caused by topographic variations. In rare cases of a particularly rough sample or accentuated geometry, the trajectories are so perturbed that the topography may be visible in a polarization image. In such cases, provision has been made in the spin analyzer of Fig. 2.38 for the electron beam to scatter from a low atomic number graphite target which can be rotated into position in place of the Au target. The difference between the image taken using the graphite target and the Au target is then the true polarization.

2.3.1.3 Examples of Magnetization Images

Each spin analyzer determines the secondary electron polarization and intensity at each point as the SEM beam rasters the sample. The intensity measurement gives the topographic map as in a conventional SEM. The polarization measurement, (2.82), gives two components of the polarization. Multiplying the polarization map by -1 , one obtains an image of the magnetization in direction and relative magnitude. The SEMPA image processing system has to be able to perform image processing tasks such as data storage and display, filtering and background subtraction, line scans, and other standard tasks like image rotation and expansion. Additionally, because magnetization is a vector quantity, the image processing system has to combine the components of magnetization in various ways to best display the magnetization vector field. The simplest display is of each magnetization component individually as in Fig. 2.39a and b where M_x and M_y of a region on the (001) surface of a Fe single crystal whisker are shown. The gray scale gives the direction for each component. Thus, in Fig. 2.39a white indicates magnetization to the right and black to the left. In the M_y image of Fig. 2.39b white indicates magnetization in the upward direction. For an Fe(001) surface there are two in plane easy axes of magnetization along [100] type directions. The intermediate gray levels in the diamond at the center of the M_y image of Fig. 2.39b correspond to magnetization in the x direction. The difference in the gray levels shows that the magnetization axes are not exactly aligned with the axes of the spin analyzer.

The image of Fig. 2.39 is a relatively large area, low magnification (250 \times) scan of the Fe whisker. Typically, such an image would be acquired with a 60 nA beam that is 250 nm in diameter. The image is 256 \times 192 pixels and was acquired in 4 min. The time for image acquisition varies widely depending on the purpose, that is, on the pixel density and statistics required. When selecting the desired area on the sample to image, a 64 \times 48 pixel scan in 3 s makes it easy to position the sample and scan area. A typical image in routine work would be 256 \times 192

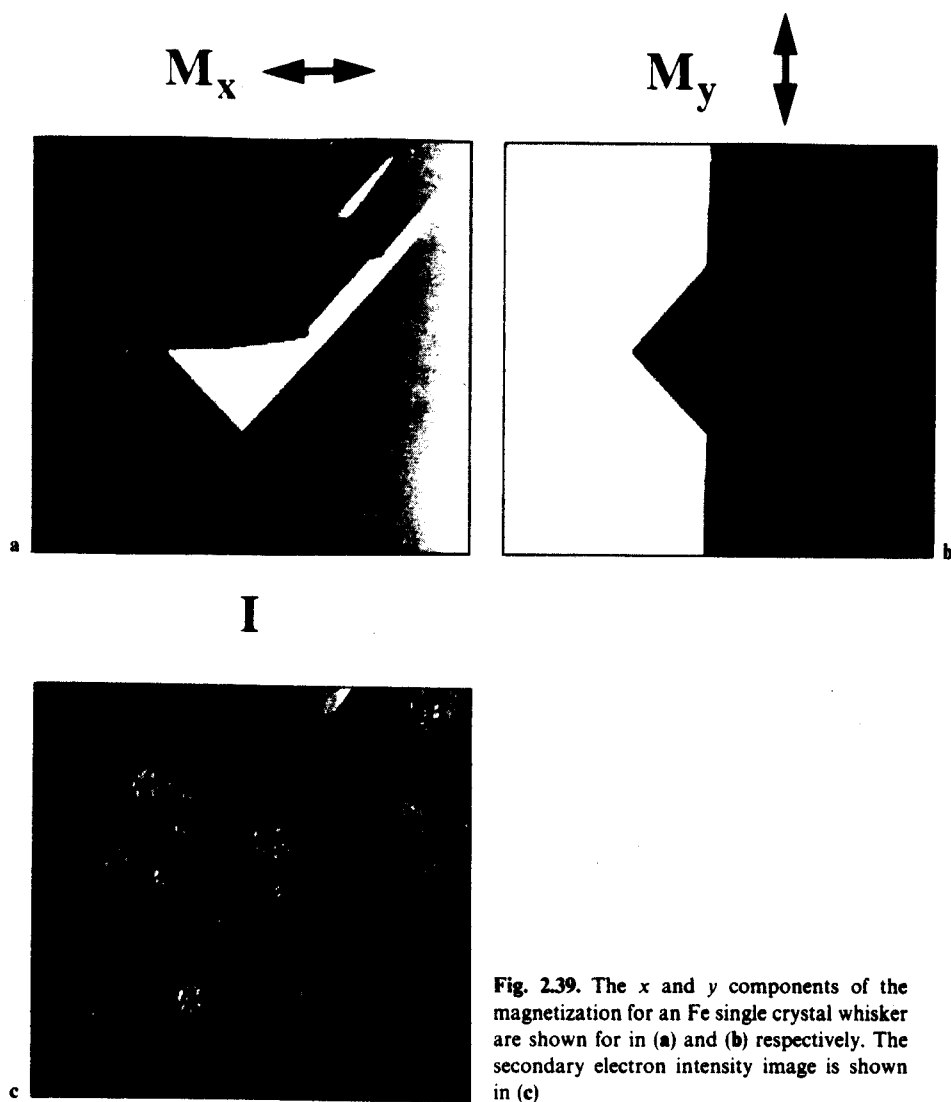


Fig. 2.39. The x and y components of the magnetization for an Fe single crystal whisker are shown for in (a) and (b) respectively. The secondary electron intensity image is shown in (c)

pixels and would take about 10 min. For samples with low magnetization contrast and where highest pixel resolution is required, 512×384 pixel scans lasting up to 100 min have been made. Over this long time period some drift in position, for example due to the sample stage, may be observed in high magnification images.

In a conventional SEM image, the intensity of the secondary electrons gives an image which reflects the topography of the sample. The spin analyzer directly measures the intensity which is the sum of the current to opposing quadrants,

the denominators in (2.82a, b). The intensity image corresponding to M_x is shown in Fig. 2.39c; the intensity image measured with M_y is identical. Because the intensity is measured simultaneously with the polarization but independent of it, the magnetization and the topographic images can be separated allowing

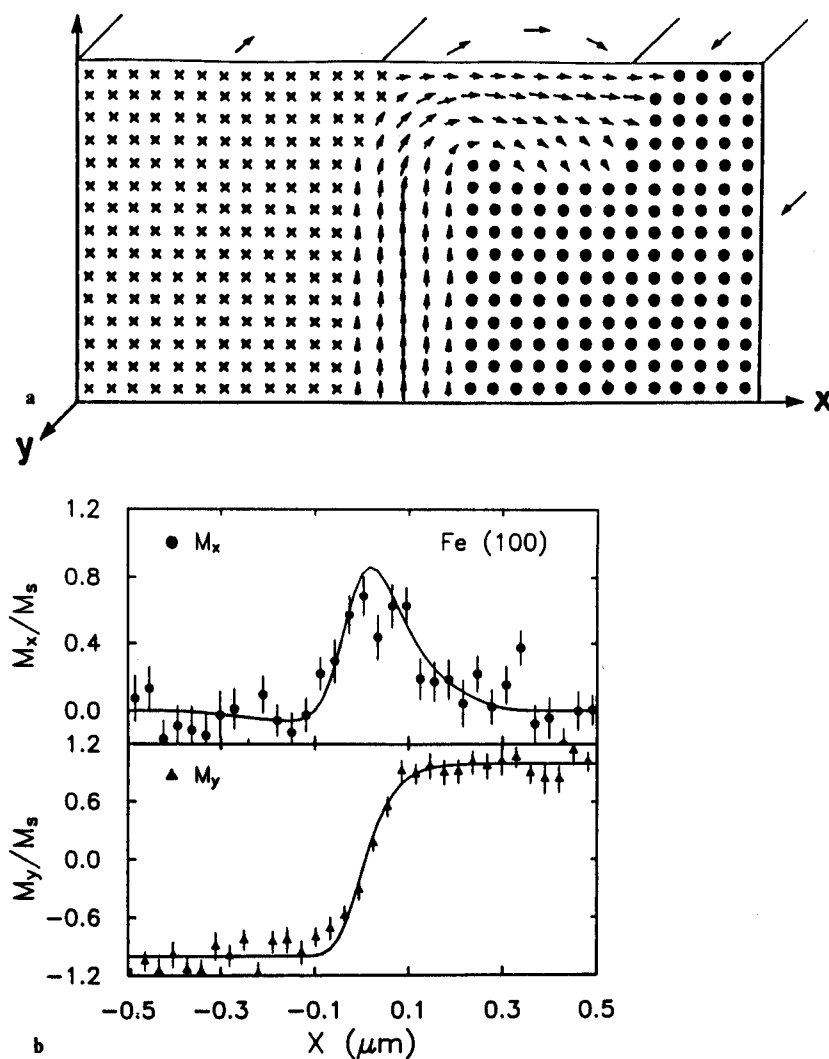


Fig. 2.40. (a) Schematic representation of calculated magnetization distribution in a cross section through the upper part of an Fe sample. The domain wall is a Bloch wall in the solid, but rotates into a Néel wall at the surface (from [2.179]). (b) Measurements of the x and y components of magnetization relative to the saturation magnetization M_s are shown in the upper and lower panels respectively versus distance in the x direction. The data were acquired with a beam current of 0.3 nA. The solid line is the result of micromagnetic theory convolved with the measured beam current (70 nm FWHM) density distribution. (From [2.191])

the investigation of the influence of the topography on the magnetic structure. For example, SEMPA has been used to observe the pinning of domain walls by point defects in a magnetic sample [2.189].

It is sometimes useful to present the magnetization information in other ways. For example, the angle between the x axis and the direction of the magnetization in the surface plane is

$$\Theta_{\text{in-plane}} = \tan^{-1}(M_y/M_x). \quad (2.83)$$

The direction of magnetization can be displayed in a color image where, through a color wheel, each color is associated with a direction. For the Fe whisker shown in Fig. 2.39 there is no out-of-plane magnetization owing to the cost in magnetostatic energy. An example of a material where SEMPA has been used to measure all three components of the magnetization is Co where there is a strong uniaxial anisotropy perpendicular to the Co(0001) surface [2.190]. The angle of the magnetization relative to the surface is

$$\Theta_{\text{out-of-plane}} = \tan^{-1}[M_z/(M_x^2 + M_y^2)^{1/2}]. \quad (2.84)$$

A useful check on the data is to form the quantity

$$|M| = (M_x^2 + M_y^2 + M_z^2)^{1/2}, \quad (2.85)$$

which should be a constant. This is indeed the case, although depending on the beam diameter there may be some "missing magnetization" at a domain wall. This is just an artifact which arises when the beam diameter is greater than the wall width and the oppositely directed polarization measured on each side of the wall adds to zero.

When domain walls are examined at high resolution, we obtain [2.191] results like those in Fig. 2.40 for a 180° wall in Fe. In order to understand the measurements, we first show the results of a magnetic microstructure calculation. Figure 2.40a shows a schematic representation of the calculated magnetization distribution in the upper $0.2 \mu\text{m}$ of an Fe sample. The sample has two domains with magnetization in the $+y$ and $-y$ directions. The cross section in the $x-z$ plane shows how the Bloch wall separating the domains is perpendicular to the surface inside the sample but turns over into a Néel wall at the surface. Line profiles of the relative magnetization M_x/M_s and M_y/M_s along the x direction are shown in Fig. 2.40b. Note the asymmetry of the surface Néel wall. The calculation, broadened to account for the electron beam diameter, shown by the solid line is seen to be in good agreement with the experimental results. When required, SEMPA has very high resolution capability even to the point of investigating domain wall structure.

2.3.1.4 Summary of SEMPA Features and Comparison to Other Imaging Techniques

Several features of SEMPA make it particularly suited to the investigation of exchange coupled layers. The features of SEMPA will be summarized and

compared to other techniques used to investigate magnetic microstructure. SEMPA directly measures the direction and relative magnitude of the magnetization *vector*. Most methods used for observing magnetic microstructure are sensitive to the magnetic fields associated with ferromagnetic materials. For example, decoration of domain walls with fine magnetic particles as in the *Bitter* method rely on fringing fields at domain walls [2.192]. In Lorentz microscopy, either in transmission or reflection, magnetic contrast comes from the deflection of the electron beam by the magnetic induction inside the material or emanating from it [2.172, 193]. Only the magneto-optic Kerr effect also directly measures the relative magnetization of the sample by determining the change in the polarization of light upon reflection [2.194, 195].

SEMPA has very high spatial resolution, 50 nm in the instrument used in this work and higher in instruments employing SEMs with field emission cathodes [2.185, 186]. Only transmission Lorentz microscopy has higher spatial resolution, ≤ 10 nm, but the sample must be thinned to less than about 300 nm thick which can change the magnetization distribution. Differential phase contrast microscopy [2.196] and electron holography [2.197] are variations on transmission Lorentz microscopy which have the similarity that their response is to the magnetic flux density integrated over the thickness of the sample. As is demonstrated in Sect. 2.32, the ability of SEMPA to observe the magnetization in thin film structures on an extremely high quality substrate, like the Fe single crystal whisker, is crucial to the investigation.

The surface sensitivity of SEMPA, which is approximately 1 nm and can be an obstacle to overcome in some investigations, is a very useful feature for investigating exchange coupled layers. As will be seen, it is possible to observe the magnetization of the top layer of an Fe/Cr/Fe(001) sandwich and determine its coupling to the substrate without any interfering signal from the substrate. Furthermore, the sample preparation and measurement can be done *in situ*. In contrast, Kerr microscopy has a probing depth of the order of 10 nm and a contribution to the signal from the substrate cannot be avoided. Also, samples must be coated with a protective layer and removed from the preparation chamber to the optical microscope for optimum resolution (200 nm) Kerr microscopy. A disadvantage of SEMPA is its sensitivity to magnetic fields which makes it impossible to apply a field to obtain a measure of the strength of the coupling as can be done in a magneto-optic Kerr measurement (*Bader and Erskine*, Chap. 4).

Another significant advantage of SEMPA is that it is possible to separate magnetic from topographic contrast which can be a source of confusion in other imaging methods. In fact, one can look for correlations that would indicate an influence of the topography on the magnetization. Because the same incident electron beam can also be used for scanning Auger microscopy, it is possible to investigate the relationship between particular chemical features on the surface and the magnetization.

2.3.2 SEMPA Measurements of Exchange Coupled Multilayers

As mentioned in the introduction, multilayer structures of magnetic layers separated by nonmagnetic interlayers exhibit many interesting properties including a "giant" magnetoresistance and long-range oscillatory coupling. Many questions about the mechanism of the exchange coupling, its range, and its strength remain unanswered. In this work we focus primarily on the mechanism of the interaction. Is the pronounced periodicity of the *magnetic* coupling as a function of the interlayer thickness related to the *electronic* structure, for example, to the Fermi surface of the interlayer material? To answer this question we have prepared very high quality "sandwich" structures, in the first instance of Fe/Cr/Fe, and determined the periods of oscillation of the magnetic exchange coupling. A bilayer of magnetic and nonmagnetic material is the basic building block for a multilayered structure that could include hundreds of layers. The three layer sandwich is the limiting case of a multilayer. It has been shown that the exchange coupling strength is independent of the number of bilayers and is the same for superlattice and sandwich structures [2.198].

2.3.2.1 The Fe/Cr/Fe(001) Sample

Theoretical investigations of magnetic coupling deal with perfect crystals of magnetic and nonmagnetic materials with a sharp interface between them. In making a comparison to theory, it is important that experimental artifacts like imperfect crystallinity, defects, interface roughness, and interdiffusion, be minimized. We describe here in some detail our attempts to grow Fe/Cr/Fe sandwiches which approach the idealized structures of theory. The single crystal Fe whisker substrate, the geometry and growth of the Cr interlayer, and the characterization of the growth and determination of the thickness are all important aspects of the sample preparation for investigation of the magnetic exchange coupling using SEMPA.

The Fe single crystal whiskers have (100) faces and approximately square cross sections. They are typically several hundred μm in width and a centimeter or two in length. Iron whiskers are extremely high-quality crystals with a very low dislocation density [2.199]. RHEED patterns show an arc of spots expected from a perfect crystal and seen only in measurements of other high-quality crystal faces such as cleaved GaAs and high temperature annealed Si(111). The whisker surfaces are naturally flat from growth. Scanning tunneling microscopy measurements of Fe(100) whisker surfaces show that there is a distance of about 1 μm between each single-atom-high step [2.200]. This corresponds to an alignment of the surface to the (100) plane to better than 0.01° which cannot be achieved on a metal surface by mechanical polishing. Furthermore, the surface is strain free. The absence of strain is also apparent in the magnetic microstructure. Strains in the whisker, for example, near an end of the whisker that is clamped, show up as very irregular domain patterns. The SEMPA measurements of the

exchange coupling are facilitated by having a region of the surface consisting of two oppositely directed domains running along the length of the whisker; a SEMPA measurement is used to select suitable whiskers.

The lattice constant of Cr, $a_{\text{Cr}} = 0.2885$ nm, is well-matched to that of Fe, $a_{\text{Fe}} = 0.2866$ nm, and would be expected to grow in registry with the Fe substrate with a small contraction of the Cr lattice in the plane of the film of somewhat less than 0.7%. Both are body-centered cubic crystals at room temperature. The desired mode of film growth is the Frank-van der Merwe mode in which each layer is completed before the next starts, that is, layer-by-layer growth. In a quasi-equilibrium situation where the temperature is high enough that the deposited atoms can diffuse to low energy sites, the following relation must hold:

$$\gamma_{\text{Cr}} + \gamma_i + \gamma_e - \gamma_{\text{Fe}} \leq 0, \quad (2.86)$$

where γ_{Cr} and γ_{Fe} are the surface free energies of the film and the substrate, γ_i is the interface free energy, and γ_e is the strain energy [2.201]. For first layer growth, γ_i is the interface free energy for the Fe-Cr interface and is small and negative [2.202], and for subsequent layers it goes to zero for the homoepitaxial growth of Cr on Cr [2.201]. Estimates of the surface free energies vary considerably [2.202, 203] but that of Cr is consistently less than that of Fe, indicating the possibility of layer-by-layer growth of Cr on Fe. The lattice mismatch is small and the strain energy, γ_e , is also small. The growth of Fe on Cr is not expected to be such a good example of layer-by-layer growth. However, some roughness in the final Fe film does not affect the investigation of the coupling as we show that the coupling period is not sensitive to the thickness of the final Fe overlayer.

A careful investigation of the exchange coupling as a function of interlayer thickness requires measuring many identical films differing only by small increments of thickness. The preparation of many films individually is tedious, and reproducibility in relative thickness and film quality is difficult to achieve. An alternative method which has proven highly successful [2.204-207] is to grow a film linearly increasing in thicknesses, that is in a wedge, such that all thicknesses in that range are accessible. A schematic of such a Cr wedge interlayer is shown in Fig. 2.41. We obtained the wedge-shaped Cr interlayer by moving a precision piezo-controlled shutter during the Cr evaporation. The wedge area was typically a few hundred μm wide by a few hundred μm long. Over this small region, it was easier to ensure sample homogeneity and quality than for a large sample. The ability of the SEM to measure such a small sample is one of its great advantages.

The first step in preparing the Fe/Cr/Fe(001) sample shown in Fig. 2.41 was to clean the Fe whisker [2.208] by 2 keV Ar ion bombardment at 750°C. Following this initial cleaning, the surface could be recleaned by a brief ion bombardment at room temperature followed by a 800°C anneal. Sputter damage is removed and a smooth, flat surface is recovered by annealing. After annealing, the principle contaminant, which was oxygen, was below about 0.05 monolayer (ML). The Cr was evaporated from a bead of Cr that had been

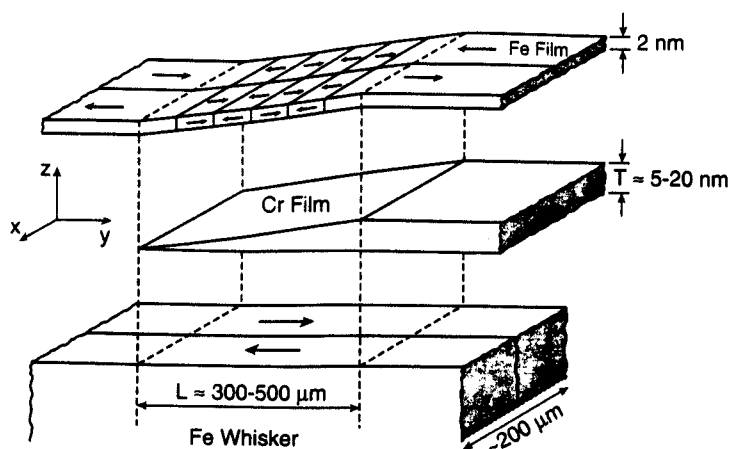


Fig. 2.41. A schematic expanded view of the sample structure showing the Fe(001) single-crystal whisker substrate, the evaporated Cr wedge, and the Fe overlayer. The arrows in the Fe show the magnetization direction in each domain. The z -scale is expanded approximately 5000 times. (From [2.206])

electroplated on a 0.25 mm diameter W wire [2.209]. Different evaporation rates were used, ranging from 1 to 12 ML per minute. These were achieved with filament currents of 7–9 A and produced minimal outgassing. An Auger spectrum of the Cr wedge just after evaporation revealed 0.01 ML of oxygen. There was no apparent correlation between the time the Cr was exposed to residual gas contaminants before being covered by the Fe overlayer and the behavior of the magnetic coupling. The Fe overlayer was electron beam evaporated from a pure Fe rod at rates of approximately 10 ML per minute to a thickness ranging from about 0.5 to 2 nm. The magnetization of the Fe overlayer could be monitored by SEMPA during evaporation allowing one to observe the appearance of the domain pattern due to the coupling through the Cr to the substrate. This domain pattern was independent of Fe overlayer thickness over the range tested (approximately 0.7–3 nm). Usually the Fe overlayer was evaporated onto the Cr layer at a substrate temperature of 50–100 °C.

The temperature of the Fe whisker substrate during evaporation of the Cr wedge is crucial to the quality of growth of the Cr film which in turn has a profound effect on the interlayer exchange coupling. The first indication of differences in the structural quality of films grown at two different temperatures was from observations of the RHEED patterns. The RHEED pattern of the clean Fe substrate exhibits an arc of spots as expected for an ideal crystal, and Kikuchi lines are also visible. If the Cr is evaporated on the Fe substrate at temperatures of 300–350 °C, the RHEED pattern remains as an arc of spots with an additional very slight streaking. On the other hand, if the substrate is in the neighborhood of 100 °C or below, during the Cr evaporation the sharp RHEED

pattern changes to broad streaks with some indication of 3d growth. In a separate experiment, Scanning Tunneling Microscopy (STM) observations have confirmed [2.200] that the high temperature growth proceeds layer-by-layer, but the low temperature growth produces a growth front containing five to six layers.

Measurements of the RHEED intensity as a function of thickness also provide a means to determine the thickness very precisely. The dashed curve in Fig. 2.42 shows the intensity of the specular RHEED beam measured during deposition of the first 15 layers of Cr evaporated in the thick part of a Cr wedge with the Fe substrate at 350°C. The electron beam was incident 3–4° from the surface and 2° off the [100] azimuth. The diffraction was near to the out-of-phase condition such that diffraction from one layer high Cr islands interfered destructively with the Fe substrate. When the Cr reaches a half layer coverage, the RHEED intensity is at a minimum and increases to a maximum as the layer fills in to completion. This process is repeated with each layer to give the cusp-like oscillations observed which are indicative of layer by layer growth [2.210]. In the SEM, it is also possible to measure the RHEED intensity after deposition by scanning the SEM beam along the Cr wedge. The solid curve in Fig. 2.42 shows the oscillations in RHEED intensity as the beam is scanned along the first part of the same Cr wedge sample which when measured during deposition gave the dashed curve. Note the similarity in the shape of the oscillations indicating that the growth at each instant in time is frozen at a point in space and revealed in the solid curve. The electron beam has to be scanned beyond the nominal zero thickness value to reach the bare substrate. This is due to the penumbra, the extent of which is known from the extended evaporation source and the distance of the shutter from the whisker. We use these spatial RHEED intensity oscillations to provide a precise measure of the thickness of the Cr film.

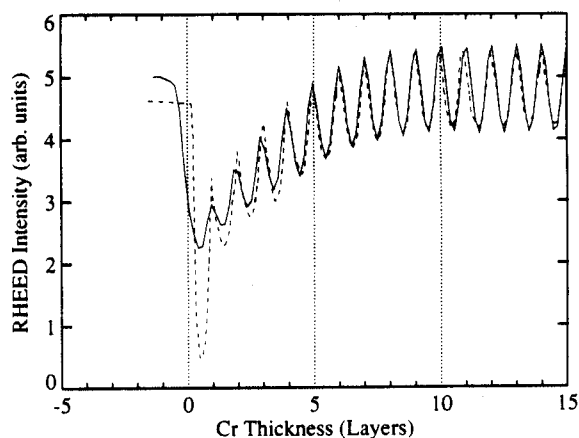


Fig. 2.42. RHEED intensity oscillations measured as a function of time during the growth of a Cr film on Fe(001) are shown by the dashed line. Spatial RHEED intensity oscillations measured as the electron beam is scanned along the wedge after deposition are shown by the solid line

2.3.2.2 SEMPA Observations of Interlayer Exchange Coupling

SEMPA measures very directly whether the Fe overlayer is ferromagnetically or antiferromagnetically coupled to the Fe whisker through a given thickness. First, the magnetization in the substrate is measured, and then, after the sandwich structure is grown, the magnetization in the Fe overlayer, separated by the Cr interlayer of varying thickness [2.206], is measured. As a first example, Fig. 2.43a shows the SEMPA magnetization image of the clean Fe whisker substrate. In this section we use the coordinates of Fig. 2.41. The region of interest on the whisker has two domains along the length of the whisker. The magnetization, in the upper domain is in the $+y$ direction (white) and that of the lower domain is in the $-y$ direction (black). The domains in the top Fe layer of a Fe/Cr/Fe(001) sandwich for a Cr wedge evaporated at a substrate temperature of 30°C are displayed in the magnetization image shown in Fig. 2.43b. The coupling starts off ferromagnetic, that is the magnetization in the Fe overlayer is in the same direction as the substrate below. At a Cr thickness of about three layers, the coupling between the Fe layers changes from ferromagnetic to antiferromagnetic. This continues to reverse through several oscillations as the Cr interlayer thickness increases. The period or wavelength of the oscillations varies from 1.6 to 1.9 nm of Cr thickness, equivalent to a thickness of 11–13 Cr layers. Note that the scale on Fig. 2.43 is the thickness of the Cr interlayer which increases from zero at the left of Fig. 2.43b to 11 nm at the right over a distance of approximately 0.5 mm on the Fe whisker. In the region where the Cr interlayer is thicker the exchange coupling is less well defined as indicated by the irregular domains.

The sensitivity of the exchange coupling to the quality of the Cr interlayer is strikingly demonstrated in Fig. 2.43c which shows the domains in the Fe overlayer of an Fe/Cr/Fe(001) sandwich in the case where the Cr wedge was grown with the substrate at 350°C . The coupling is initially ferromagnetic and switches to antiferromagnetic at five layers. However, in contrast to the coupling through a Cr wedge grown at lower temperature, the coupling through Cr grown at higher temperature is seen to change, after the initial ferromagnetic coupling region, with each layer of Cr giving a period of oscillation of nearly two layers. We say "nearly" because between 24 and 25, 44 and 45, and 64 and 65 layers, indicated by arrows at the top of the figure, no reversal takes place. This corresponds to a phase slip resulting from the accumulation of a phase difference owing to the incommensurability of the exchange coupling period and the lattice constant. This oscillatory exchange coupling continues through 75 layers (over 10 nm) of Cr.

The persistence of the short-period oscillations with increasing interlayer thickness is closely correlated with the interlayer roughness as indicated by RHEED intensity oscillations. Growth at lower temperatures, 250°C for example, allows roughness to build up more in the Cr wedge such that in one instance the short-period oscillations were not observed beyond a thickness of about 30 ML. A particularly vivid example of the correlation between the

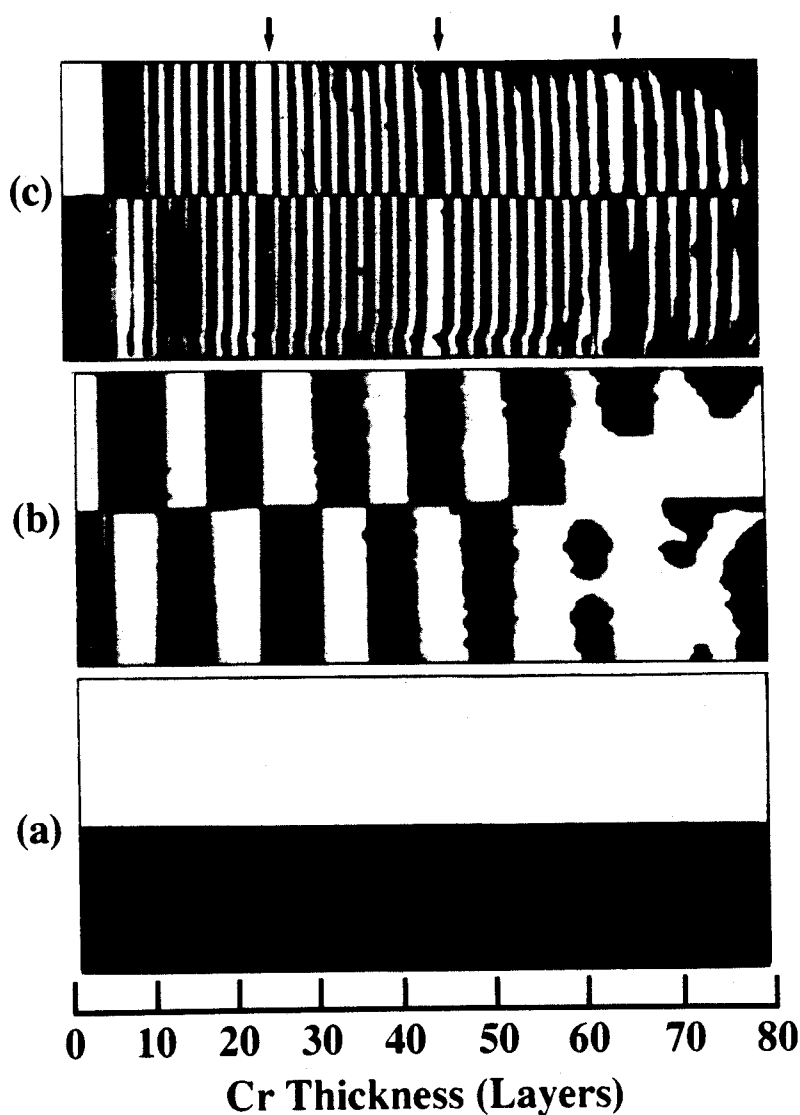


Fig. 2.43. SEMPA image of the magnetization M_y (axes as in Fig. 2.41) showing domains in (a) the clean Fe whisker, (b) the Fe layer covering the Cr spacer layer evaporated at 30°C, and (c) the Fe layer covering a Cr spacer evaporated on the Fe whisker held at 350°C. The scale at the bottom shows the increase in the thickness of the Cr wedge in (b) and (c). The arrows at the top of (c) indicate the Cr thicknesses where there are phase slips. The region of the whisker imaged is about 0.5 mm long

RHEED intensity oscillations and the short-period oscillations in the exchange coupling is seen in Fig. 2.44. In Fig. 2.44a an image of the RHEED intensity is shown as the SEM beam is rastered over a Cr wedge grown at 250°C. We attribute the absence of RHEED oscillations in the lower right part of the image

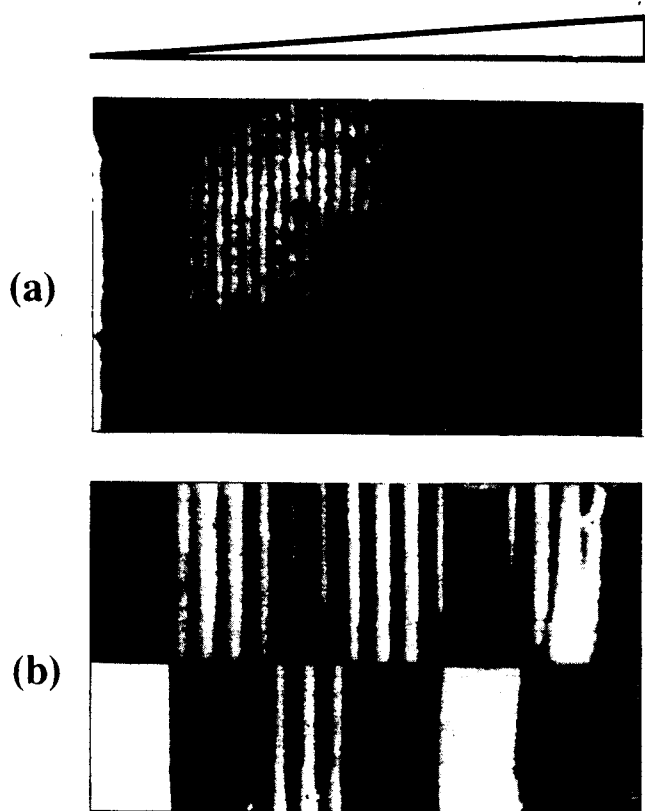


Fig. 2.44. The effect of roughness on the interlayer exchange coupling is shown by a comparison of (a) the oscillations of the RHEED intensity along the bare Cr wedge with (b) the SEMPA magnetization image over the same part of the wedge

to roughness of the Cr interlayer, probably induced by damage in the Fe substrate which had been sputtered and annealed many times. However, the important point to note is that in the magnetization image of the Fe overlayer in Fig. 2.44b the coupling reverts to oscillatory coupling with a long-period exactly where the RHEED intensity oscillations are absent.

It is noteworthy that a calculation [2.156] of the exchange coupling in Fe/Cr/Fe predicted short-period oscillations, in addition to the long-period oscillations, before short-period oscillations had been observed experimentally. Wang et al. [2.156] pointed out that the apparent discrepancy with experiment could be accounted for by interface roughness corresponding to the displacement of one quarter of the atoms in an interface by one layer. For a position on the wedge n layers thick, this roughness corresponds to 25% of the surface being at $n - 1$ layers, 50% at n layers, and 25% at $n + 1$ layers. This is equivalent to a three layer growth front of the Cr with 0.1 nm rms roughness. We see the need,

in order to observe the short-period oscillations, to approach more closely ideal layer-by-layer growth where one layer is completed before the next begins.

We now take a closer look at the exchange coupling observed in Fig. 2.43c. Measurements of the bare Cr wedge [2.173], before the Fe overlayer was deposited to obtain the magnetization image of Fig. 2.43c, are shown in Fig. 2.45a-c. The RHEED intensity oscillations used to determine the wedge thickness are shown in Fig. 2.45a. Such a line scan is taken from an image of the RHEED intensity as in Fig. 2.44a. Also apparent in this image are features in the topography of the Fe whisker surface which are replicated in the wedge. These features are compared to their counterparts in the SEMPA intensity image to bring the RHEED and SEMPA images into registry. In this way, the RHEED provides an atomic layer scale to determine the wedge thickness. The build up of disorder and roughness with increasing wedge thickness is indicated by the corresponding decrease in the amplitude of the RHEED intensity oscillations in Fig. 2.45a.

The measured spin polarization of secondary electrons from the bare Cr is shown in Fig. 2.45b. The high polarization of electrons from the Fe at the start of the wedge decreases exponentially as the Fe electrons are attenuated by the Cr film of increasing thickness. A fit to the exponential gives a $1/e$ sampling depth for SEMPA in Cr of 0.55 ± 0.04 nm. Subtracting an exponential leaves the polarization of the Cr alone which is shown magnified by a factor of 4 in Fig. 2.45c. Because of the attenuation of electrons coming from layers below the

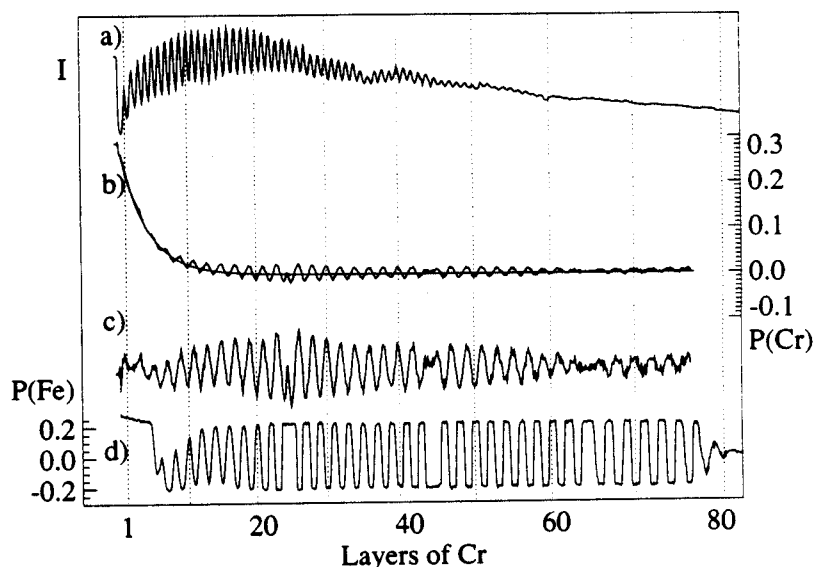


Fig. 2.45. (a) RHEED intensity oscillations determine the thickness of the Cr wedge deposited on the Fe whisker. (b) The spin polarization $P(\text{Cr})$ of secondary electrons emitted from the Cr wedge. (c) Data of (b) after subtracting the exponential shown and multiplying by 4. (d) The spin polarization, $P(\text{Fe})$, from the Fe overlayer deposited on the Cr wedge of (a-c). (From [2.173])

surface, the measured polarization, $P(\text{Cr})$, is dominated by the polarization of the surface layer which is seen to reverse approximately every layer.

When the Fe overlayer was added to this Cr wedge we obtained the image of Fig. 2.43c from which we can also get a profile of the polarization, $P(\text{Fe})$, shown in Fig. 2.45d. The initial coupling between the Fe layers is ferromagnetic and reverses at five layers. The polarization of the Fe overlayer is seen to be opposite to that of the top Cr layer before deposition. This observation is consistent with spin polarized photoemission [2.211] and electron energy loss measurements [2.212] which have found that the Cr interface layer couples antiferromagnetically to Fe. With this coupling at each interface and if the Cr orders antiferromagnetically with alternating planes of aligned spins for layer stacking in the [001] direction, one expects Fe layers separated by an even (odd) number of layers of Cr to be coupled antiferromagnetically (ferromagnetically). However, from Fig. 2.45d we see that Fe separated by seven layers of Cr is coupled antiferromagnetically, opposite to expectations. A close examination of Fig. 2.45c reveals that there is a "defect" in the antiferromagnetic layer stacking of Cr between one and four layers. That is, at a thickness of less than four layers, two adjacent layers of Cr must have parallel moments.

The short-period oscillations in the interlayer exchange coupling in Fe/Cr/Fe have been attributed [2.156] to an RKKY-type interaction through paramagnetic Cr. The asymptotic form of the RKKY interaction at a distance z from a plane of ferromagnetic moments [2.213] is $\sin(k_s z)/(k_s z)^2$ where for a free-electron gas the Fermi surface spanned by the wave vector k_s is just the Fermi sphere so $k_s = 2k_F$. In the case of Fe/Cr/Fe, we are interested in the exchange coupling, $J(nd)$, between two planes of moments separated by the Cr interlayer of thickness nd

$$J(nd) \propto \sin(k_s nd)/(k_s nd)^2. \quad (2.87)$$

Here the distinction is made that the thickness does not vary continuously but in monolayer steps, nd , where d is the layer spacing. The phase slips seen in Fig. 2.43c and Fig. 2.45d occur because the wave vector k_s governing the oscillations is incommensurate with the lattice wave vector, $2\pi/a = \pi/d$. The measure of the incommensurability, δ , gives the fraction of a lattice wave vector by which the spanning wave vector differs from the lattice wave vector, i.e. $k_s = (1 - \delta)\pi/d$. The oscillatory part of the interaction can then be written

$$J(nd) \propto \sin[(\pi/d)(1 - \delta)nd] = -(-1)^N \sin(N\delta\pi). \quad (2.88)$$

The interaction is seen to change sign with each layer and to be modulated by an envelope function with period $N = 2/\delta$. There is a node in the function $\sin(N\delta\pi)$ every δ^{-1} layers. There is an accumulation of phase $\delta\pi$ with each additional layer of Cr with a phase slip of one layer after 20 layers corresponding to $\delta = 0.05$, and $k_s = 0.95\pi/d$.

Chromium is very special in that there is strong "nesting" of the Cr Fermi surface [2.214]. Here an extended region of one part of the Fermi surface is

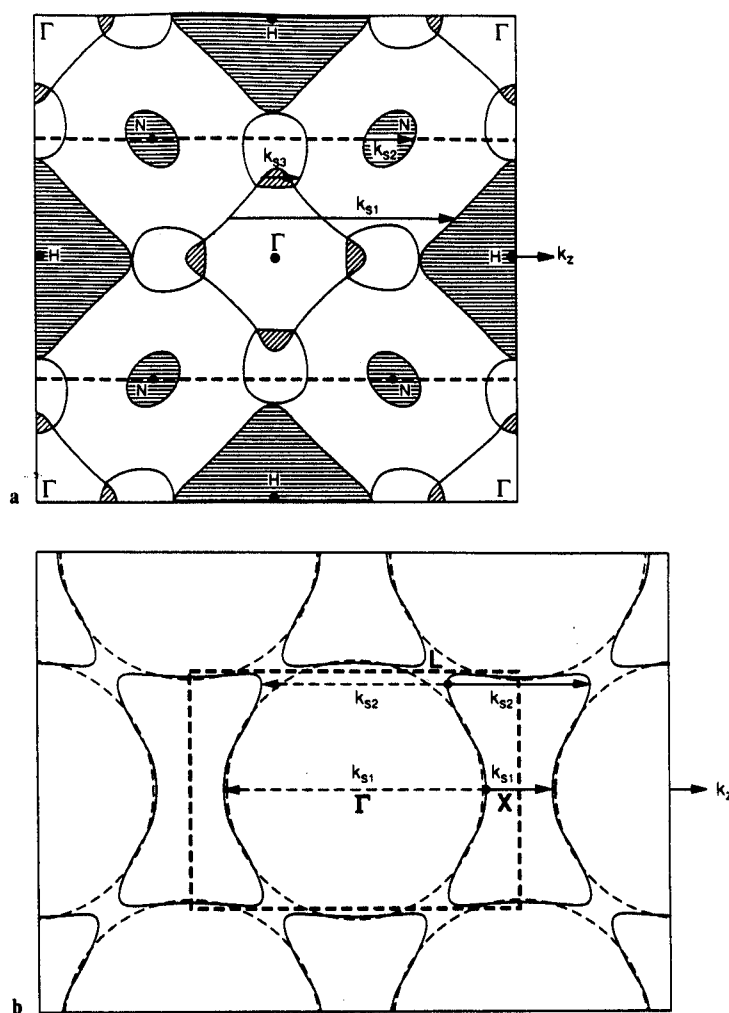


Fig. 2.46. Cuts through the Brillouin zone which contain the z direction of the layer stacking are shown for (a) Cr (from [2.214]) and (b) Ag (from [2.217]). The heavy dashed lines show the interface-adapted first Brillouin zone. The k_s which give rise to oscillations in the magnetic coupling are shown. The light dashed circles in (b) indicate a free electron Fermi surface

parallel to another part separated by the spanning wave vector k_{s1} as shown in Fig. 2.46a. The susceptibility is strongly enhanced at this k_s which leads to strong short-period oscillatory interlayer exchange coupling in the RKKY picture. The same enhanced susceptibility at k_{s1} leads to spin density wave (SDW) antiferromagnetism in bulk Cr below the Néel temperature, T_N [2.215]. This makes it hard to distinguish between an RKKY-like coupling and an explanation where the magnetization in the Fe overlayer is locked to the

antiferromagnetism of the Cr. However, our measurements of the short-period oscillations in the interlayer exchange coupling of Fe/Cr/Fe(001) spanned the temperature range from T_N to $1.8T_N$, over which bulk Cr is *paramagnetic*. This would suggest that either the coupling takes place through paramagnetic Cr or that the presence of the Fe substrates stabilizes antiferromagnetism in Cr even above the bulk Néel temperature.

To further investigate the coupling mechanism, we have analyzed the magnetization images of the bare Cr wedge to obtain $P(\text{Cr})$ of Fig. 2.45c. The same phase slips in the oscillations of the coupling of the Fe overlayer are also observed in $P(\text{Cr})$ at Cr thicknesses of 24–25, 44–45, and 64–65 layers. Thus Cr/Fe(001) exhibits incommensurate SDW behavior within the Cr film; this behavior has also been observed over the temperature range from T_N to $1.8T_N$. Although thermal fluctuations destroy SDW antiferromagnetism in bulk Cr above T_N , it appears that the Fe substrate establishes a SDW in the Cr film some distance from the interface. There are two closely related ways to view this response in the Cr film. In one view, since even above T_N the magnetic susceptibility is enhanced at the nesting wave vector, an antiferromagnetic response can be induced in the Cr by the presence of the Fe. Alternatively, if the Cr is viewed as paramagnetic, RKKY-like oscillations would be established which would be quite similar to the antiferromagnetic order because both derive from the same strong Fermi surface nesting.

The origin of the mechanism giving rise to coupling with long-period oscillations is less clear. There are two spanning vectors of the Cr Fermi surface, $k_{s,2}$ and $k_{s,3}$ in Fig. 2.46a, which give periods of 1.35 and 1.62 nm [2.216] which are comparable to the 1.6–1.9 nm observed. However, Cr with its unfilled-bands has at least 11 spanning vectors where there is significant Fermi surface nesting [2.216] and one has to argue why only two periods of oscillation are observed. We have seen how the roughness associated with low temperature growth can destroy short-period oscillations in the magnetic coupling. Furthermore, it must be remembered that the nesting is only part of the story; the matrix elements, which have not as yet been calculated, undoubtedly play an important role.

Although Fe/Cr/Fe has been an important system in which the antiferromagnetic coupling and subsequently oscillations were first observed, deriving conclusions about the mechanism of the exchange coupling is more complicated because of the SDW-antiferromagnetism and the complex Fermi surface of Cr. It is useful then to consider another interlayer material, like Ag, which is not an antiferromagnet and which has a much simpler Fermi surface as shown in Fig. 2.46b. The Fermi surface is nearly spherical with necks at the L points in $[111]$ directions [2.217]. There are just two nesting vectors which would be expected to lead to coupling in the $[001]$ direction which can be seen in the (110) cut through the Brillouin zone shown in the figure. These are shown by the dashed lines, $k_{s,1}$ across the diameter of the “sphere” and $k_{s,2}$ connecting portions of the Fermi surface at the necks. Because the structure is periodic in the z direction with layer spacing, d , a reciprocal lattice vector $2\pi/d$ can be added or subtracted to k_s , to give for example the $k_{s,1}$ and $k_{s,2}$ shown by the solid

lines in Fig. 2.46b which connect the same points on the Fermi surface as the dashed k_z . The period corresponding to k_{z1} is not a short-period less than $2d$ which would be possible in a free-electron gas, but rather the period is

$$\lambda = 2\pi / [(2\pi/d) - k_{z1}]. \quad (2.89)$$

This difference between the free electron gas and the multilayer structure has been discussed and variously referred to as the vernier effect or aliasing by the periodic lattice planes [2.157, 159, 163]. The periods predicted [2.157] from the bulk Fermi surface of Ag are $\lambda_1 = 5.58d$ and $\lambda_2 = 2.38d$, where for bulk Ag the layer spacing is $d = 0.204$ nm.

We have investigated [2.174] the interlayer exchange coupling in Fe/Ag/Fe(001) using the procedures described above for Fe/Cr/Fe(001) differing only in Ag evaporation rate and temperature of the Fe whisker during evaporation. However, the growth is not as good and there is significant mismatch in the growth direction. Nevertheless, the oscillations of the exchange coupling persists to thicknesses of over 50 ML (> 10 nm). We observed 23 reversals in the magnetization. There is variation in the spacing between reversals which immediately shows that more than one period of oscillation was present. To extract these periods from the data, a Fourier transform of the data was carried out which revealed two periods that were used as the initial values for the periods in a fitting program. The data was modeled by adding two sine waves with these periods and with adjustable phases and amplitudes. This continuous function was discretized with the Ag lattice. Then all positive coupling values were set to the same magnetization value and negative coupling values were set to an equal but opposite magnetization, thereby simulating the effect of the Fe overlayer. The coupling period determined from varying the parameters to achieve the best fit are $\lambda_1 = 5.73 \pm 0.05t_0$ and $\lambda_2 = 2.37 \pm 0.07t_0$. The experimentally determined coupling periods are in excellent agreement with the theoretical values of $5.58t_0$ and $2.38t_0$ considering possible uncertainties in the theory and the possibility of slight tetragonal distortions in the Ag film. The SEMPA measurements show that the oscillations of the interlayer exchange coupling in Fe/Ag/Fe(001) are consistent with theories in which oscillation periods are derived from Fermi surface spanning vectors.

It is interesting to compare our results with interlayers of Cr and Ag in epitaxial structures with results from sputtered multilayers where the interface is not coherent and generally rougher. *Parkin* [2.218] and Sect. 2.4, has reported results of study of multilayer structures of 18 different transition or noble metal spacer materials between Co layers. The sputtered multilayers were polycrystalline, textured (111), (110), and (0001) for fcc, bcc, and hcp, respectively. For the eight interlayer materials which showed oscillation in the coupling, each material except Cr has a single oscillation period of 1.0 ± 0.1 nm. The similarity of the periods for quite different materials has led many to the conclusion that this long-period coupling does not derive from Fermi surface properties.

In contrast to the studies of sputtered samples, studies of epitaxially grown structures show a variety of periods. Besides our SEMPA studies Fe/Cr/Fe,

which we have discussed at length, others have found evidence for two periods of oscillation in Fe/Cr/Fe(001) [2.204, 207]. Two periods of oscillation have also been found in Co/Cu/Co(001) [2.219], Fe/Au/Fe(001) [2.220], and of course in our SEMPA measurements of Fe/Ag/Fe(001) [2.174]. Additionally, short-period oscillations in the magnetic coupling have been observed for Fe/Cu/Fe(001) [2.219], Fe/Mo/Fe(001) [2.221], Fe/Mn/Fe(001) [2.222], and Fe/Pd/Fe(001) [2.223]. In each case, the observed periods of oscillation of the magnetic coupling have been related to Fermi surface spanning vectors. This is particularly striking in the case of the (001) films of the noble metals for which two periods are expected from Fermi surface nesting, as we discussed for Ag. In each case, two periods are observed which agree quite well with Fermi surface predictions.

How can these results from epitaxially grown structures be reconciled with those from sputter deposited multilayers? Recently, *Stiles* [2.216] has calculated the degree of the Fermi surface nesting of the fcc, bcc and hcp transition metals for which oscillatory coupling was observed by *Parkin* in the sputtered multilayers. Because of the complicated nature of the Fermi surfaces and the large number of spanning vectors, it is possible to identify in each case a spanning vector that could give rise to the observed oscillation. If the observed periods can be attributed to Fermi surface spanning vectors, the alternative question is why periods are not observed which correspond to the several other k_s for which there is Fermi surface nesting? First, as we discussed for Cr, the matrix elements which would give the strength of the coupling at each k_s are not known and could be quite small. Second, as illustrated so vividly in the case of Fe/Cr/Fe(001) by Figs. 2.43, 44, roughness at an interface can completely wash out short-period oscillations.

2.3.2.3 Biquadratic Coupling

The coupling of two Fe layers through Cr has been discussed thus far in terms of the component of magnetization along the whisker, M_y , in the coordinates of Fig. 2.41. The coupling is seen to be ferromagnetic or antiferromagnetic in nature, depending on the Cr layer thickness, leading to images of an oscillatory coupling as seen in Fig. 2.43. As discussed in Sect. 2.3.1, the other in-plane component of magnetization, M_x , is measured simultaneously. Both components are shown in Fig. 2.47 in a region of wedge thickness from 20 to 30 ML which includes a phase slip. At thicknesses where M_y reverses, the other component of magnetization, M_x , is observed. that is, an additional coupling which tries to hold the magnetization of the two Fe layers perpendicular to each other is manifested. One of the many ways of writing the total coupling energy is [2.205, 224]

$$E = A_{12}[1 - \mathbf{m}_1 \cdot \mathbf{m}_2] + 2B_{12}[1 - (\mathbf{m}_1 \cdot \mathbf{m}_2)^2], \quad (2.90)$$

where \mathbf{m}_1 and \mathbf{m}_2 are unit vectors in the direction of magnetization of the two Fe

layers. Within a constant, the first term is proportional to $\cos \theta_{12}$ and the second to $\cos^2 \theta_{12}$, where θ_{12} is the angle between \mathbf{m}_1 and \mathbf{m}_2 .

The first term in (2.90) is the bilinear coupling which we have emphasized thus far, where J has been replaced by A_{12} ; for positive (negative) A_{12} it is a

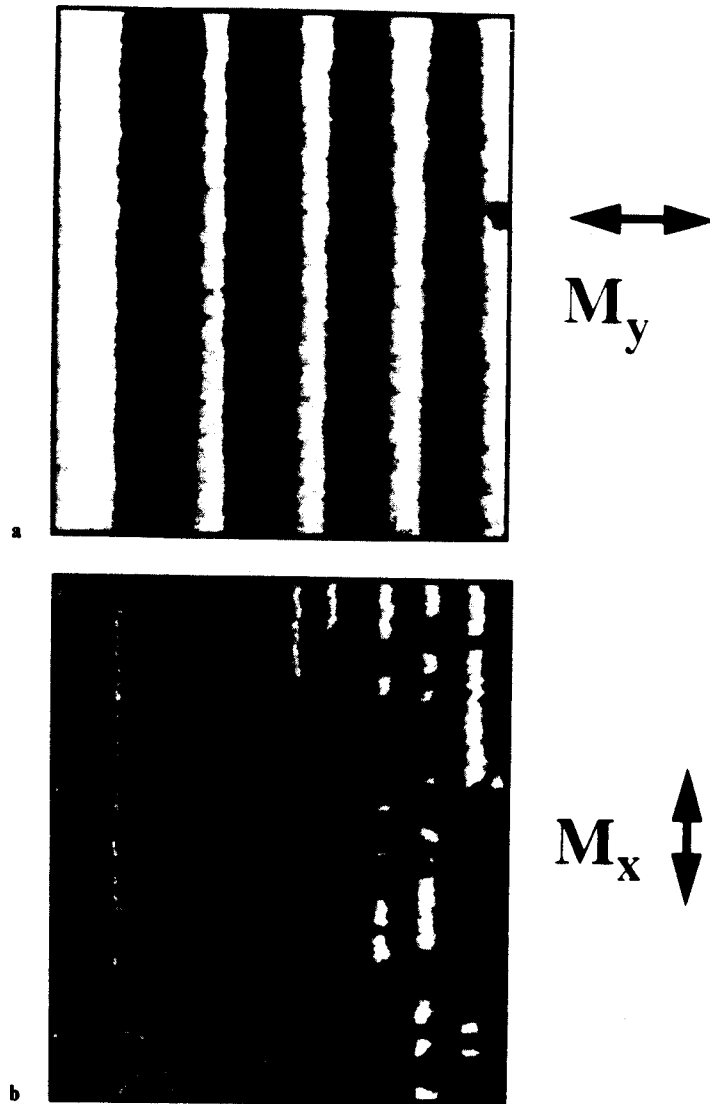


Fig. 2.47. The SEMPA magnetization images (a) M_y and (b) M_x are shown for that region of a Fe/Cr/Fe(001) trilayer over which the Cr thickness varies from 20 to 30 layers. A phase slip lies in this thickness range. The biquadratic coupling is evident from the strong contrast in the M_x image. (From [2.206])

minimum for m_1 and m_2 parallel (antiparallel). The second term is the biquadratic term; for negative B_{12} it is a minimum when m_1 and m_2 are perpendicular. The coupling is usually dominated by the bilinear term except at transitions from ferromagnetic to antiferromagnetic coupling where A_{12} goes through zero. At these thicknesses, the biquadratic term dominates and magnetic domains oriented along the x axis which are orthogonal to the domains of the Fe whisker substrate, are observed as in Fig. 2.47. The transition regions are not simply domain walls in the Fe film, but are much wider and scale in width with the slope of the Cr wedge. This perpendicular coupling was first observed for Fe/Cr/Fe and attributed to biquadratic coupling in a magneto-optic Kerr microscopy investigation of Fe/Cr/Fe sandwich structures [2.205].

Slonczewski [2.225] has proposed a theory which attributes the biquadratic coupling to fluctuations in the bilinear coupling caused by fluctuations in the thickness in the Cr interlayer. In general, there are fluctuations in the bilinear coupling near the transition thickness at which the coupling changes sign. There will be both the regions of ferromagnetic coupling, and at slightly different thickness on the other side of the transition, antiferromagnetic coupling. In the case of Cr films grown at elevated temperatures, the fluctuations are just the short period part of the interlayer exchange coupling. Thus, at a Cr thickness of $n + \frac{1}{2}$ layers, where the bilinear coupling makes a transition from ferromagnetic to antiferromagnetic coupling, there are many microscopic regions with n or $n + 1$ layers giving rise to fluctuations owing to the different bilinear coupling at the two thicknesses. The exchange of coupling within the Fe overlayer resists there being many magnetization reversals over microscopic spatial dimension as would be dictated by the fluctuations in the bilinear coupling, and the energy is

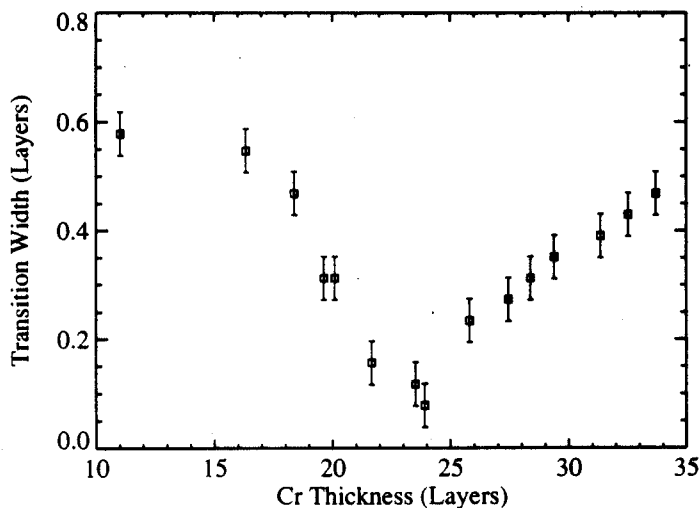


Fig. 2.48. Measurement of the width of the transition region (10–90% of M_y) for the switching of the bilinear coupling as a function of thickness of the Cr film

lowered by the magnetic moments turning in a direction perpendicular to the competing bilinear coupling directions.

In this theory, B_{12} is proportional to $(\Delta J)^2$ where $\pm \Delta J$ represents the fluctuation in the bilinear exchange coupling. One consequence of this fluctuation model of the biquadratic coupling is that this coupling will be small when the strength ΔJ of the short-period interlayer exchange coupling interaction is small. This can be expected to occur at a phase slip where, as seen from (2.88), there is a node in the envelop function $\sin(N\delta\pi)$. The width of the biquadratic coupling regions, in fractions of a Cr layer thickness, is a measure of the relative strength of the biquadratic and bilinear coupling. This width is plotted for several transitions near a phase slip in Fig. 2.48. The diminishing width of the biquadratic coupling region measured near a phase slip is in agreement with the predictions of the *Slozcewski* model [2.225] of the biquadratic coupling.

2.3.2.4 Summary

Since the first observations [2.153] of oscillations in the exchange coupling and magnetoresistance in multilayers of Fe or Co separated by non-ferromagnetic spacer layers, it was clear that the oscillations, and in particular the periods of the oscillations, stand as beacons to guide theories of the coupling mechanism. SEMPA is especially well-suited to make a quantitative comparison of the periods of the long range oscillatory coupling with the extremal features of the spacer layer Fermi surface. The high spatial resolution of SEMPA permits the use of small, high-quality specimens. Obtaining high-quality trilayer samples on regions of nearly perfect Fe single crystal whiskers has allowed the observation of oscillation of the coupling in Fe and Ag over many periods. The surface sensitivity of SEMPA is exploited in these studies to interrogate only the top layer of a tri-layer structure. The possibility to prepare specimens *in situ* and bring other techniques to bear in the SEM, such as RHEED and Auger spectroscopy, are all important capabilities. SEMPA measurements have given the most precise determination of the periods of the oscillation of the interlayer magnetic coupling in the Fe/Cr/Fe(001) and Fe/Ag/Fe(001) systems, the two systems that have been studied by SEMPA to date. Our experimental results on Cr and Ag interlayers support theories of interlayer exchange coupling based on Fermi surface properties. The long-range coupling between the magnetic layers is determined by the electronic response of the spacer layer. The indirect exchange coupling takes place through the electrons at the Fermi surface, the same electrons which are involved in the magneto-transport and which define the Fermi surface. SEMPA measurements have led to an increased understanding of exchange coupling of magnetic layers.

Acknowledgements. This work was supported by the Technology Administration of the U.S. Department of Commerce and the Office of Naval Research. The Fe whiskers were grown at Simon Fraser University under an operating grant from the National Science and Engineering Research Council of Canada.

- 2.122 A. Vedyayev, B. Dieny, N. Ryshanova: *Europhys. Lett.* **19**, 329 (1992)
- 2.123 A. Fert, A. Barthélémy, P. Etienne, S. Lequien, R. Loloee, D.K. Lottis, D.H. Mosca, F. Petroff, W.P. Pratt, P.A. Schroeder: *J. Magn. Magn. Mater.* **104-107**, 1712-1716 (1992)
- 2.124 J. Inoue, S. Maekawa: *Prog. Theor. Phys.* **106**, 187 (1991)
- 2.125 B. Rodmacq, B. George, M. Vaezzadeh, Ph. Mangin: *Phys. Rev. B* **46**, 1206 (1992)
- 2.126 M.A.M. Gijs, M. Okada: *Phys. Rev. B* **46**, 2908 (1992)
- 2.127 D.H. Mosca: "Giant Magnetoresistance in Magnetic Materials", Thesis (Porto Alegre-Orsay, 1991)
- 2.128 F. Petroff, A. Barthélémy, A. Fert, P. Etienne, S. Lequien: *J. Magn. Magn. Mater.* **93**, 95 (1991)
- 2.129 E.E. Fullerton, D.M. Kelly, J. Guimpel, I.K. Schuller, Y. Bruynseraede: *Phys. Rev. Lett.* **68**, 859 (1992)
- 2.130 Y. Obi, K. Takanashi, Y. Mitami, N. Tsuda, H. Fujimori: *J. Magn. Magn. Mat.* **104-107**, 1747 (1992); K. Takanashi, Y. Obi, Y. Mitami, H. Fujimori: *J. Phys. Soc. Jpn.* **61**, 1169 (1992)
- 2.131 S.S.P. Parkin, Z.G. Li, D.J. Smith: *Appl. Phys. Lett.* **58**, 2710 (1991); also D. Greig, M.J. Hall, C. Hammond, B.J. Hickey, H.P. Ho, M.A. Howson, M.J. Walker, N. Wisen, D.G. Wright: *J. Magn. Magn. Mat.* **110**, 239 (1992); M.E. Tomlinson, R.J. Pollard, D.G. Lord, P.J. Grundy: *J. Magn. Magn. Mat.* **111**, 79 (1992)
- 2.132 R.J. Highmore, W.C. Shih, R.E. Sonekh, J.E. Evetts: *J. Magn. Magn. Mat.* **115** (1992)
- 2.133 Y. Saito, S. Hashimoto, K. Inomata: *Appl. Phys. Lett.* **60**, 2436 (1992)
- 2.134 J. Kohlhepp, S. Cordes, H.J. Elmers, U. Gradmann: *J. Magn. Magn. Mat.* **111**, 231 (1992)
- 2.135 B.A. Gurney, D.R. Wilhuit, V.S. Speriosu, I.L. Sanders: *IEEE Trans. Magn.* **26**, 2747 (1990)
- 2.136 P. Baumgart, B.A. Gurney, D. Wilhuit, T. Nguyen, B. Dieny, V.S. Speriosu: *J. Appl. Phys.* **69**, 4792 (1991); B.A. Gurney, P. Baumgart, D.R. Wilhuit, B. Dieny, V.S. Speriosu: *J. Appl. Phys.* **70**, 5867 (1991)
- 2.137 R. Nakatami, K. Okuda: *InterMag Conf.* (St Louis, 1992)
- 2.138 B. Dieny, V.S. Speriosu, J.P. Nozières, B.A. Gurney, A. Vedyayev, N. Ryzhanova: *Magnetism and Structure in Systems of Reduced Dimension*, ed. by R.F.C. Farrow et al. (Plenum Press, New York, 1993) p. 279
- 2.139 J.M. George, A. Barthélémy, F. Petroff, T. Valet, A. Fert: *Mat. Res. Symp. Proc. Vol. 313* (Materials Research Society 1993) p. 737
- 2.140 S. Zhang, P.M. Levy: *Phys. Rev. B* **43**, 11048 (1991)
- 2.141 J.L. Duvail, D.K. Lottis, A. Fert: *Conference on Magnetism and Magnetic Materials 1994*, to appear in *J. Appl. Phys.* 1994
- 2.142 W.P. Pratt, S.F. Lee, J.M. Slaughter, P.A. Schroeder, J. Bass: *Phys. Rev. Lett.* **66**, 3060 (1991); S.F. Lee, W.P. Pratt Jr, R. Loloee, P.A. Schroeder, J. Bass: *Phys. Rev. B* **46**, 548 (1992)
- 2.143 M. Johnson: *Phys. Rev. Lett.* **67**, 3594 (1991); M. Johnson, R.H. Silsbee: *Phys. Rev. B* **35**, 4959 (1987)
- 2.144 S. Zhang, P.M. Levy: *J. Appl. Phys.* **69**, 4786 (1991)
- 2.145 A. Fert, T. Valet: *J. Magn. Magn. Mat.* **121**, 378 (1993); T. Valet, A. Fert: *Phys. Rev. B* **48**, 7099 (1993)
- 2.146 P.A. Schroeder: *Magnetism and Structure in Systems of Reduced Dimension*, ed. by R.F.C. Farrow et al. (Plenum Press, New York, 1993) p. 129; S.F. Lee, W.P. Pratt, Q. Yang, D. Holody, R. Loloee, P.A. Schroeder, J. Bass: *J. Magn. Magn. Mat.* **118**, L1 (1993)
- 2.147 F. Nguyen Van Dau, A. Fert, M. Baibich: *J. Phys. (Paris)* **49**, C8-1663 (1988)
- 2.148 S. Zhang, P.M. Levy: *Mat. Res. Symp. Proc. Vol. 313*, (Materials Research Society 1993) p. 53

Section 2.3

- 2.149 C.F. Majkrzak, J.W. Cable, J. Kwo, M. Hong, D.B. McWhan, Y. Yafet, J.V. Waszczak, C. Vettier: *Phys. Rev. Lett.* **56**, 2700 (1986)
- 2.150 P. Grünberg, R. Schreiber, Y. Pang, M.B. Brodsky, H. Sowers: *Phys. Rev. Lett.* **57**, 2442 (1986)
- 2.151 M.N. Baibich, J.M. Broto, A. Fert, F. Nguyen Van Dau, F. Petroff, P. Etienne, G. Creuzet, A. Friederich, J. Chazelas: *Phys. Rev. Lett.* **61**, 2472 (1988)
- 2.152 G. Binasch, P. Grünberg, F. Saurenbach, W. Zinn: *Phys. Rev. B* **39**, 4828 (1989)

- 2.153 S.S.P. Parkin, N. More, K.P. Roche: Phys. Rev. Lett. **64**, 2304 (1990)
- 2.154 Y. Yafet: J. Appl. Phys. **61**, 4058 (1987)
- 2.155 C. Kittel: "Indirect Exchange Interactions in Metals", in *Solid State Physics*, ed. by F. Seitz, D. Turnbull, H. Ehrenreich (Academic, New York, 1968), Vol. 22, p. 1
- 2.156 Y. Wang, P.M. Levy, J.L. Fry: Phys. Rev. Lett. **65**, 2732 (1990)
- 2.157 P. Bruno, C. Chappert: Phys. Rev. Lett. **67**, 1602 (1991); Phys. Rev. B **46**, 261 (1992)
- 2.158 F. Herman, J.R. Schrieffer: Phys. Rev. B **46**, 5806 (1992)
- 2.159 R. Coehoorn: Phys. Rev. B **44**, 9331 (1991)
- 2.160 W. Baltensperger, J.S. Helman: Appl. Phys. Lett. **57**, 2954 (1990)
- 2.161 D.M. Edwards, J. Mathon, R.B. Muniz, M.S. Phan: J. Phys. Condens. Matter **3**, 4941 (1991)
- 2.162 K.B. Hathaway, J.R. Cullen: J. Magn. Magn. Mat. **104-107**, 1840 (1992)
- 2.163 D.M. Deaven, D.S. Rokhsar, M. Johnson: Phys. Rev. B **44**, 5977 (1991)
- 2.164 D. Stoeffler, F. Gautier: Prog. Theor. Phys. Suppl. **101**, 139 (1990)
- 2.165 H. Hasegawa: Phys. Rev. B **42**, 2368 (1990)
- 2.166 F. Herman, J. Sticht, M. Van Schilfgaarde: Mat. Res. Soc. Symp. Proc. **231**, 195 (1992)
- 2.167 J. Unguris, D.T. Pierce, A. Galejs, R.J. Celotta: Phys. Rev. Lett. **49**, 72 (1982)
- 2.168 E. Kisker, W. Gudat, K. Schröder: Solid State Commun. **44**, 591 (1982)
- 2.169 H. Hopster, R. Raue, E. Kisker, G. Guntherodt, M. Campagna: Phys. Rev. Lett. **50**, 70 (1983)
- 2.170 D.R. Penn, S.P. Apell, S.M. Girvin: Phys. Rev. Lett. **55**, 518 (1985); Phys. Rev. B **32**, 7753 (1985)
- 2.171 J. Glazer, E. Tosatti: Solid State Commun. **52**, 905 (1984)
- 2.172 J.I. Goldstein, D.E. Newbury, P. Echlin, D.C. Joy, C. Fiori, E. Lifshin: *Scanning Electron Microscopy and X-ray Microanalysis* (Plenum, New York, 1984)
- 2.173 J. Unguris, R.J. Celotta, D.T. Pierce: Phys. Rev. Lett. **69**, 1125 (1992)
- 2.174 J. Unguris, R.J. Celotta, D.T. Pierce: J. Magn. Magn. Mat., **127**, 205 (1993)
- 2.175 R.J. Celotta, D.T. Pierce: *Microbeam Analysis-1982*, ed. by K.F.J. Heinrich (San Francisco Press, San Francisco) p. 469
- 2.176 K. Koike, H. Matsuyama, K. Hayakawa: Scanning Micros. Suppl. **1**, 241 (1987)
- 2.177 G.G. Hembree, J. Unguris, R.J. Celotta, D.T. Pierce: Scanning Micros. Suppl. **1**, 229 (1987)
- 2.178 M.R. Scheinfein, J. Unguris, M.H. Kelley, D.T. Pierce, R.J. Celotta: Rev. Sci. Instrum. **61**, 2501 (1990)
- 2.179 J. Unguris, M.R. Scheinfein, R.J. Celotta, D.T. Pierce: "Scanning Electron Microscopy with Polarization Analysis: Studies of Magnetic Microstructure", in *Chemistry and Physics of Solid Surfaces VIII*, ed. by R. Vanselow, R. Howe (Springer, Berlin, Heidelberg, 1990) p. 239
- 2.180 J. Unguris, D.T. Pierce, R.J. Celotta: Rev. Sci. Instrum. **57**, 1314 (1986)
- 2.181 D.T. Pierce, R.J. Celotta, M.H. Kelley, J. Unguris: Nucl. Instrum. Meth. A **266**, 550 (1988)
- 2.182 J. Kessler: *Polarized Electrons*, 2nd ed. (Springer, Berlin, Heidelberg, 1985)
- 2.183 K. Koike, K. Hayakawa: Jpn. J. Appl. Phys. **23**, L187 (1984)
- 2.184 J. Unguris, G.G. Hembree, R.J. Celotta, D.T. Pierce: J. Microscopy **139**, RP1 (1985)
- 2.185 R. Allenspach, M. Stampanoni, A. Bischof: Phys. Rev. Lett. **65**, 3344 (1990)
- 2.186 H.P. Oepen, J. Kirschner: Scanning Micros. **5**, 1 (1991)
- 2.187 R. Jungblut, C. Roth, F.U. Hillebrecht, E. Kisker: Surf. Sci. **269/270**, 615 (1992)
- 2.188 M.R. Scheinfein, D.T. Pierce, J. Unguris, J.J. McClelland, R.J. Celotta: Rev. Sci. Instrum. **60**, 1 (1989)
- 2.189 D.T. Pierce, J. Unguris, R.J. Celotta: MRS Bulletin **13**, 19 (1988)
- 2.190 J. Unguris, M.R. Scheinfein, R.J. Celotta, D.T. Pierce: Appl. Phys. Lett. **55**, 2553 (1989)
- 2.191 M.R. Scheinfein, J. Unguris, J.L. Blue, K.J. Coakley, D.T. Pierce, R.J. Celotta, P.J. Ryan: Phys. Rev. **43**, 3395 (1991)
- 2.192 F. Bitter: Phys. Rev. **38**, 1903 (1931)
- 2.193 J.P. Jacobovics: "Lorentz Microscopy and Applications (TEM and SEM)", in *Electron Microscopy in Materials Science Part IV*, ed. by E. Ruedl, U. Valdre (Commission of European Communities, Brussels, 1973) p. 1303
- 2.194 W. Rave, R. Schafer, A. Hubert: J. Magn. Magn. Mater. **65**, 7 (1987)
- 2.195 B.E. Argyle, B. Petek, D.A. Herman, Jr.: J. Appl. Phys. **61**, 4303 (1987)
- 2.196 J.N. Chapman, S. McVitie, J.R. McFadyen: Scanning Micros. Suppl. **1**, 221 (1987)

- 2.197 A. Tonomura: J. Appl. Phys. **61**, 4297 (1987)
- 2.198 S.S.P. Parkin, A. Mansour, G.P. Felcher: Appl. Phys. Lett. **58**, 1473 (1991)
- 2.199 P.D. Gorsuch: J. Appl. Phys. **30**, 837 (1959)
- 2.200 D.T. Pierce, J. Strosio, J. Unguris, R.J. Celotta: Phys. Rev. B **49** (1994)
- 2.201 E. Bauer, J.H. van der Merwe: Phys. Rev. B **33**, 3657 (1986)
- 2.202 A.R. Miedema: Z. Metallk. **69**, 287 (1978); **69**, 455 (1978)
- 2.203 L.Z. Mezey, J. Giber: Jpn. J. Appl. Phys. **21**, 1569 (1982)
- 2.204 S. Demokritov, J.A. Wolf, P. Grünberg, W. Zinn: in Proc. Mater. Res. Soc. Symp. **231**, 133 (1992)
- 2.205 M. Rührig, R. Schäfer, A. Hubert, R. Mosler, J.A. Wolf, S. Demokritov, P. Grünberg: Phys. Status Solidi (a) **125**, 635 (1991)
- 2.206 J. Unguris, R.J. Celotta, D.T. Pierce: Phys. Rev. Lett. **67**, 140 (1991)
- 2.207 S.T. Purcell, W. Folkerts, M.T. Johnson, N.W.E. McGee, K. Jager, J. aan de Stegge, W.B. Zeper, W. Hoving, P. Grünberg: Phys. Rev. Lett. **67**, 903 (1991)
- 2.208 S.T. Purcell, A.S. Arrott, B. Heinrich: J. Vac. Sci. Technol. B **6**, 794 (1988)
- 2.209 J.J. McClelland, J. Unguris, R.E. Scholten, D.T. Pierce: J. Vac. Sci. Technol., A **11**, 2863 (1993)
- 2.210 M.G. Lagally, D.E. Savage, M.C. Tringides: in *Reflection High-Energy Electron Diffraction and Reflection Electron Imaging of Surfaces*, ed. by P.K. Larsen, P.J. Dobson, NATO ASI Series B188 (Plenum Press, New York, 1988) p. 139
- 2.211 F.U. Hillebrecht, C. Roth, R. Jungblut, E. Kisker, A. Bringer: Europhys. Lett. **19**, 711 (1992)
- 2.212 T.G. Walker, A.W. Pang, H. Hopster, S.F. Alvarado: Phys. Rev. Lett. **69**, 1121 (1992)
- 2.213 Y. Yafet: Phys. Rev. B **36**, 3948 (1987)
- 2.214 D.G. Laurent, J. Calloway, J.L. Fry, N.E. Brener: Phys. Rev. B **23**, 4977 (1981)
- 2.215 E. Fawcett: Rev. Mod. Phys. **60**, 209 (1988)
- 2.216 M. Stiles: Phys. Rev. B **48**, 7238 (1993)
- 2.217 D. Shoenberg, D.J. Roaf, Philos. Trans. R. Soc. London **255**, 85 (1962)
- 2.218 S.S.P. Parkin: Phys. Rev. Lett. **67**, 3598 (1991)
- 2.219 M.T. Johnson, S.T. Purcell, N.W.E. McGee, R. Coehoorn, J. aan de Stegge, W. Hoving: Phys. Rev. Lett. **68**, 2688 (1992)
- 2.220 A. Fuss, S. Demokritov, P. Grünberg, W. Zinn: J. Magn. Magn. Mater. **103**, L221 (1992)
- 2.221 Z.Q. Qiu, J. Pearson, A. Berger, S.D. Bader: Phys. Rev. Lett. **68**, 1398 (1992)
- 2.222 S.T. Purcell, M.T. Johnson, N.W.E. McGee, R. Coehoorn, W. Hoving: Phys. Rev. B **45**, 13064 (1992)
- 2.223 Z. Celinski, B. Heinrich: J. Magn. Magn. Mater. **99**, L25 (1991)
- 2.224 P. Grünberg, S. Demokritov, A. Fuss, R. Schreiber, J.A. Wolf, S.T. Purcell: J. Magn. Magn. Mater. **104-107**, 1734 (1992)
- 2.225 J.C. Slonczewski: Phys. Rev. Lett. **67**, 3172 (1991)

Section 2.4

- 2.226 T. Shinjo, T. Takada: "Metallic Superlattices", in *Ferromagnetic Materials*, Vol. 3, ed. by E.P. Wohlfarth (Elsevier, Amsterdam, 1987)
- 2.227 I.K. Schuller: "The Physics of Metallic Superlattices: An Experimental Point of View", in *Physics, Fabrication, and Applications of Multilayered Structures*, ed. by P. Dhez, C. Weisbuch (Plenum, New York, 1988) p. 139
- 2.228 *Magnetic Properties of Low-Dimensional Systems II*, ed. by L.M. Falicov, F. Meija-Lira, J.L. Moran-Lopez (Springer, Berlin, Heidelberg, 1990)
- 2.229 L.M. Falicov, D.T. Pierce, S.D. Bader, R. Gronsky, K.B. Hathaway, H.J. Hopster, D.N. Lambeth, S.S.P. Parkin, G. Prinz, M. Salamon, I.K. Schuller, R.H. Victoria: J. Mat. Res. **5**, 1299 (1990)
- 2.230 R.E. Walstedt, J.H. Wernick: Phys. Rev. Lett. **20**, 856 (1968)
- 2.231 J.B. Boyce, C.P. Slichter: Phys. Rev. B **13**, 379 (1976)
- 2.232 L.R. Walker, R.E. Walstedt: Phys. Rev. B **22**, 3816 (1980)
- 2.233 R.M. White, *Quantum Theory of Magnetism*, (Springer, Berlin, Heidelberg, 1983)
- 2.234 J.-C. Bruyere, O. Massenet, R. Montmory, L. Néel: C.R. Acad. Sci. **258**, 1423 (1964)